



저작자표시-비영리-변경금지 2.0 대한민국

이용자는 아래의 조건을 따르는 경우에 한하여 자유롭게

- 이 저작물을 복제, 배포, 전송, 전시, 공연 및 방송할 수 있습니다.

다음과 같은 조건을 따라야 합니다:



저작자표시. 귀하는 원저작자를 표시하여야 합니다.



비영리. 귀하는 이 저작물을 영리 목적으로 이용할 수 없습니다.



변경금지. 귀하는 이 저작물을 개작, 변형 또는 가공할 수 없습니다.

- 귀하는, 이 저작물의 재이용이나 배포의 경우, 이 저작물에 적용된 이용허락조건을 명확하게 나타내어야 합니다.
- 저작권자로부터 별도의 허가를 받으면 이러한 조건들은 적용되지 않습니다.

저작권법에 따른 이용자의 권리는 위의 내용에 의하여 영향을 받지 않습니다.

이것은 [이용허락규약\(Legal Code\)](#)을 이해하기 쉽게 요약한 것입니다.

[Disclaimer](#)

공학박사학위논문

공기저항 저감을 위한
Ahmed Reference Model 주변 유동의
Synthetic Jet 능동 제어 연구

Active Control of Flow over an Ahmed Reference
Model for Aerodynamic Drag Reduction using
Synthetic Jet

2013 년 8 월

서울대학교 대학원
기계항공공학부
박 훈 일

**공기저항 저감을 위한 Ahmed Reference Model
주변 유동의 Synthetic Jet 능동 제어 연구**

**Active Control of Flow over an Ahmed Reference
Model for Aerodynamic Drag Reduction using
Synthetic Jet**

지도교수 이 동 호

**이 논문을 공학박사 학위논문으로 제출함
2013 년 4 월**

**서울대학교 대학원
기계항공공학부
박 훈 일**

**박훈일의 공학박사 학위논문을 인준함
2013 년 6 월**

위 원 장 : _____

부위원장 : _____

위 원 : _____

위 원 : _____

위 원 : _____

Abstract

Active Control of Flow over an Ahmed Reference Model for Aerodynamic Drag Reduction using Synthetic Jet

Hoonil Park

School of Mechanical and Aerospace Engineering

Seoul National University

This paper presents experimental studies on synthetic jet, a promising active flow control method for aerodynamic drag reduction. As a preliminary study, parametric study on synthetic jet actuator performance was conducted and optimization procedure was followed. And then, synthetic jet was applied to an Ahmed reference model for aerodynamic drag reduction.

A performance of synthetic jet actuator can be indicated by the maximum jet velocity, which is affected by actuator geometry and driving signal. In this study, nine synthetic jet actuator configurations were examined according to the orifice length and cavity depth (5, 10 and 15 *mm* for each), and jet velocity was measured according to driving frequency. From the result, two resonances were observed, cavity resonance and diaphragm resonance. Because actuation near the mechanical resonance may cause destruction of diaphragm, the former resonance is more important in present experiments and need to be properly used to increase the jet velocity. For most of actuator configurations, the maximum velocity was observed at cavity resonance

frequency. However, for a small cavity depth (5 mm), the jet velocity was not decreased after the cavity resonance frequency, but rather increased a little. In general, the smaller orifice length and cavity depth, the maximum jet velocity increases. But, optimum length exists for orifice length.

The synthetic jet was employed to control flow over an Ahmed reference model of which slant angles are 25° and 35°. Synthetic jet was emanated from roof end edge and slant side edges in a form of an array. The wind tunnel tests were performed according to jet direction, jet momentum coefficient, driving frequency, and number and position of activated jet within the actuator array. Total aerodynamic drag coefficient was measured, and rear wake flows were studied by tuft visualization and rear surface pressure distribution measurement. From the result, the aerodynamic drag of 25° slanted model is decreased by the jets from roof end edge at 5.2% of maximum reduction, but it is unchanged by the jets from slanted side edges. On the other hand, the aerodynamic drag of 35° slanted model is increased regardless of jet location. Particularly, it is drastically increased by the jets from roof end edge above 20% with inducing strong streamwise vortices. For drag reduced cases (25° slanted model with jets from roof end edge), the aerodynamic drag was decreased more with stronger jet and smaller jet angle relative to the free stream. But, the jet driving frequency has no direct effect on aerodynamic drag over the tested range. And the aerodynamic drag was decreased less with a fewer synthetic jet actuators, but it is effectively reduced when the activated jets are concentrated on the central parts of the roof end edge. From this research, it was found that the aerodynamic drag of car-like simplified body can be reduced by synthetic jet actuation, and the installation and driving condition of synthetic jet for aerodynamic drag reduction was revealed. But the aerodynamic drag can be drastically increased by

inappropriate application of synthetic jet.

Key Words: Active flow control, Synthetic jet, Ahmed body, Aerodynamic
drag reduction, Wind tunnel test

Student Number: 2008-20747

Table of Contents

Abstract	I
Nomenclature	VI
List of Tables	VIII
List of Figures	IX
Chapter 1. Introduction	1
1.1 Motivation.....	1
1.2 Background and Previous Researches	2
1.2.1 Automobile Aerodynamics.....	2
1.2.2 Flow Control for Aerodynamic Drag Reduction	3
1.2.3 Synthetic Jet as a Means of Flow Control	4
1.3 Previous Researches.....	6
1.3.1 Synthetic Jet Flow	6
1.3.2 Applying Synthetic Jet on Automobile.....	7
1.4 Dissertation Objective and Outline	8
Chapter 2. Description of Experiment.....	16
2.1 Wind Tunnel and Experimental Model.....	16
2.2 Measurement and Flow Visualization.....	18
2.3 Data Acquisition	22
Chapter 3. Design of Synthetic Jet Actuator	26
3.1 Experimental Setup	26
3.1.1 Perpendicular Synthetic Jet Actuator.....	26
3.1.2 Measurement System.....	28
3.1.3 Experimental Parameters	28
3.2 Parametric Study on Parallel Synthetic Jet Actuator.....	30
3.2.1 Effect of Jet Driving Frequency on Jet Velocity	30
3.2.2 Effect of Actuator Geometry on Jet Velocity	31
3.3 Optimal Design of Parallel Synthetic Jet Actuator	33
3.3.1 Design Problem Formulation.....	33
3.3.2 Artificial Neural Network.....	34
3.3.3 Optimization Result.....	35

Chapter 4. Active Control of Flow over an Ahmed Reference Model using Synthetic Jet	49
4.1 Experimental Setup.....	49
4.1.1 Experimental Model.....	49
4.1.2 Perpendicular Type Synthetic Jet Actuator	51
4.1.3 Measurement System.....	53
4.1.4 Experimental Parameters	54
4.2 Flow without Synthetic Jet Actuation	55
4.3 Flow with Synthetic Jet Actuation	57
4.3.1 Aerodynamic Drag Measurement.....	57
4.3.2 Flow Visualization: Tuft Method	60
4.3.3 Rear Surface Pressure Measurement	61
4.3.4 Tests for the Number and Position of the Activated Jet in the Actuator Array	63
Chapter 5. Conclusions	85
References	88
초 록	95

Nomenclatures

English Symbols

A, B, n	constants in King's law
A_j	orifice area of synthetic jet actuator
A_0	frontal area of wind tunnel model
AFC	active flow control method
ANN	artificial neural network
ANOVA	analysis of variance
c	speed of sound
C_D	drag coefficient
$C_{D,base}$	drag coefficient without synthetic jet actuation
C_p	static pressure coefficient
C_μ	momentum coefficient of synthetic jet
CTA	constant temperature anemometry
d_c	cavity diameter of synthetic jet actuator
d_o	orifice diameter of synthetic jet actuator
D	aerodynamic drag
DAQ	data acquisition
DO	deterministic optimization
DOE	design of experiment
DOT	design optimization tool
E	voltage in King's law
f_D	mechanical resonance frequency
f_c	cavity resonance frequency
F^+	non-dimensional jet driving frequency
h, l, w	height, length, and width of wind tunnel model
h_0	Orifice length

h_c	cavity depth of synthetic jet actuator
h_o	orifice length of synthetic jet actuator
\bar{I}_j	time-averaged momentum during the blowing stroke
n	number of synthetic jet actuators
Re_l	Reynolds number based on model length
RMSE	root mean squared error
$u_j(t)$	jet velocity of the synthetic jet
U_0	free-stream velocity of wind tunnel speed
V	velocity in King's law
V_c	cavity volume of synthetic jet actuator

Greek Symbols

θ_{jet}	angle between synthetic jet and freestream
θ_s	rear slant angle of Ahmed reference model
$\theta_{s, crit.}$	critical rear slant angle of Ahmed reference model
λ	spacing ratio of actuator spanwise spacing-to-orifice diameter
μ	dynamic viscosity
ρ_a	free-stream density
ρ_j	density of the synthetic jet
τ	half period of synthetic jet

List of Tables

Table 1.1 Regulation on automobile fuel efficiency and CO ₂ emission [2]	9
Table 3.1 Experimental parameters for synthetic jet actuator design	37
Table 3.2 Cavity resonance frequency and maximum jet velocity for each actuator configuration	38
Table 3.3 Reliability of ANN model (Analysis of variance).....	39
Table 3.4 Optimized parameters of synthetic jet actuator	39
Table 4.1 Range of experimental parameters	66
Table 4.2 Change in aerodynamic drag according to slant angle and actuator location	67
Table 4.3 Aerodynamic drag reduction according to the number and positions of activated jet actuators	68

List of Figures

Fig. 1.1 Oil price in South Korea from 1997 to 2011 [1]	10
Fig. 1.2 Streamlines in the longitudinal midsection of a Mercedes-Benz S-Class W140 series	11
Fig. 1.3 Schematic of flow past a passenger car [5]	12
Fig. 1.4 Examples of passive flow control method.....	13
Fig. 1.5 Schematic of synthetic jet actuator.....	14
Fig. 1.6 Two types of synthetic jet actuator.....	15
Fig. 2.1 Ahmed reference model configuration in original size (dimensions given in <i>mm</i>) [35]	23
Fig. 2.2 Schematic of flow over an Ahmed reference model [19].....	24
Fig. 2.3 Aerodynamic drag coefficient of Ahmed body according to the rear slant angle [31].....	25
Fig. 3.1 Components of parallel type synthetic jet actuator	40
Fig. 3.2 Final assembly of parallel type synthetic jet actuator.....	40
Fig. 3.3 Schematic of jet velocity measurement system.....	41
Fig. 3.4 Synthetic jet actuator installed in the control volume box	41
Fig. 3.5 Sample of synthetic jet velocity curve	42
Fig. 3.6 Synthetic jet velocity according to driving frequency.....	42
Fig. 3.7 Max. synthetic jet velocity according jet driving frequency at 5 <i>mm</i> of orifice length and 5, 10, 15 <i>mm</i> of cavity depth.....	43
Fig. 3.8 Max. synthetic jet velocity according jet driving frequency at 10 <i>mm</i> of orifice length and 5, 10, 15 <i>mm</i> of cavity depth	43
Fig. 3.9 Max. synthetic jet velocity according jet driving frequency at 15 <i>mm</i> of orifice length and 5, 10, 15 <i>mm</i> of cavity depth	44
Fig. 3.10 Max. synthetic jet velocity according jet driving frequency at 5, 10, 15 <i>mm</i> of orifice length and 5 <i>mm</i> of cavity depth	44
Fig. 3.11 Max. synthetic jet velocity according jet driving frequency at 5, 10, 15 <i>mm</i>	

of orifice length and 10 <i>mm</i> of cavity depth	45
Fig. 3.12 Max. synthetic jet velocity according jet driving frequency at 5, 10, 15 <i>mm</i> of orifice length and 15 <i>mm</i> of cavity depth	45
Fig. 3.13 3D contours of max. synthetic jet velocity according to the actuator geometry	46
Fig. 3.14 Construction of Artificial Neural Network (ANN) model	47
Fig. 3.15 Objective contour according to cavity depth and orifice length	47
Fig. 3.16 Objective contour according to cavity depth and jet driving frequency	48
Fig. 3.17 Objective contour according to jet driving frequency and orifice length	48
Fig. 4.1 Geometry of Ahmed body for present experiments (dimensions given in <i>mm</i>)	69
Fig. 4.2 Two rear sections according to the jet location for $\theta_s = 35^\circ$	70
Fig. 4.3 Components of perpendicular type synthetic jet actuator	71
Fig. 4.4 Final assembly of perpendicular type synthetic jet actuator	71
Fig. 4.5 Synthetic jet velocity measurements in quiescent condition	72
Fig. 4.6 Pressure ports on rear surface (dimensions given in <i>mm</i>)	73
Fig. 4.7 Schematic of wind tunnel test measurement system	74
Fig. 4.8 Wind tunnel model in SNU wind tunnel	75
Fig. 4.9 Rear wake flow of Ahmed reference model [37]	76
Fig. 4.10 Rear surface pressure distribution of a flow without synthetic jet actuation	77
Fig. 4.11 Change in aerodynamic drag by synthetic jet array actuation from roof end edge	78
Fig. 4.12 Change in aerodynamic drag by synthetic jet arrays actuation from slanted side edges	79
Fig. 4.13 Rear wake flow visualization for $\theta_s = 25^\circ$	80
Fig. 4.14 Rear wake flow visualization for $\theta_s = 35^\circ$	81
Fig. 4.15 Rear surface pressure distributions for $\theta_s = 25^\circ$ with and without synthetic jets from roof end edge	82
Fig. 4.16 Rear surface pressure distributions for $\theta_s = 35^\circ$ with and without synthetic jets from roof end edge	83

Fig. 4.17 Efficiency of jet according to the number and positions of activated jet
actuators 84

Chapter 1. Introduction

1.1 Motivation

In the midst of the oil crisis and with stringent CO₂ emission regulations, many companies and research institutes related to the automotive industry are concentrating on developing fundamental technology for improving the fuel efficiency. As shown in Fig. 1.1, the oil price in South Korea has increased rapidly for last fourteen years and the Korean government declared consolidated regulations on automobile fuel efficiency and CO₂ emission as described in Table 1.1 [1-2]. Therefore, fuel efficiency improvement of an automobile becomes more crucial. It can be improved in several ways, e.g., efficiency enhancements of the powertrain, reducing the overall weight, the use of an energy regenerative system, and a reduction in the aerodynamic drag.

Recently, there is increased concern about reducing the aerodynamic drag as vehicle speeds increase (above 120 *km/h*). Because the aerodynamic drag is proportional to the square of the vehicle speed, it accounts for much of the oil consumption and CO₂ emissions values by current transportation systems, of which large percentage are taken by cars whose owners engage in frequent high-speed driving. And, a reduction of the aerodynamic drag is achievable at a relatively low cost compared to developing a more efficient powertrain system [3]. Moreover, in the near future, engine and transmission will disappear progressively as hybrid or electric automobile era ensues. And the aerodynamics will still play an important role in automotive dynamics.

1.2 Background and Previous Researches

1.2.1 Automobile Aerodynamics

The external flow subjects the automobile to forces and moments which significantly affects the vehicle's performance, handling, safety and comfort [4]. And the aerodynamic drag (D) is one of the most important force component related to the performance of an automobile. It is, as well as the other force components and moments, increases with the square of the vehicle speed. With a typical passenger car, aerodynamic drag accounts for nearly 80 percent of the total road resistance at 100 Km/h . Therefore, the reducing the aerodynamic drag is the focal point of automobile aerodynamics to enhance the fuel efficiency or increase the speed. Generally, efforts to reduce the aerodynamic drag are concentrated on reducing the aerodynamic drag coefficient (C_D) which is closely related to the rear wake flow.

In term of fluid dynamics, automobile is a bluff body in close proximity to the ground. Its external geometry is very complex, hence the external flow also does. In the external flow of an automobile, boundary layers are turbulent and flow separation is common which may be followed by reattachment. From Fig. 1.2, it is clear that the flow past an automobile is strongly governed by separation, for example flow separation at the roof end. Fig. 1.3 provides further information on the type and location of the rear separation. In many cases, spanwise vortices emanating along with C-pillar and spanwise separation from end edge occur simultaneously [5]. For an automobile, the most of the aerodynamic loss is induced by the rear wake flow. Therefore, the

aerodynamic performance can be enhanced by controlling the rear wake flow.

1.2.2 Flow Control for Aerodynamic Drag Reduction

Flow control strategy for aerodynamic drag reduction can be divided into two primary parts, passive and active flow control method [6]. Passive flow control method is based on exterior shape design. And it also includes the additional attachment such as vortex generator and rear spoiler. Fig. 1.4 shows examples of various kinds of rear body configuration to control the rear flow of automobile for better aerodynamic performance. Streamlined body shape can reduce the pressure drag term, and angulated trunk shape, trunk kick up and rear flap can reduce the induced drag term. The Passive flow control method is widely used since 1970's and reached a mature phase now.

Recently, Active flow control technique (AFC) is emerging as an alternative solution to increase the fuel efficiency by enhancing the aerodynamic performance. AFC aims to change the overall flow field with a relatively small amount of activation energy to result in large performance gains. AFC is being spotlighted because it offers a good potential to enhance the aerodynamic performance, whereas many other types of automobile-related technologies have reached a mature phase. Therefore, development is achievable at a relatively low cost. In addition, it has advantages from an aesthetic point of view. Because AFC does not require drastic change in exterior shapes, it can improve aerodynamic performance levels with less conflict with an aesthetic designer's shape. The design of exterior shapes is a

major issue related to car sales. However, AFC is still relatively new because of the added weight and complexity to a structure. One method that has been proven an effective way to provide AFC is through the use of piezoelectric synthetic jets.

1.2.3 Synthetic Jet as a Means of Flow Control

Synthetic jet represents a promising method for flow control applications. Synthetic jet, also known as zero-net-mass-flux (ZNMF) jet, is periodical blowing and suction generated by a periodically oscillating diaphragm enclosed by walls with one or more orifices [7-9]. Synthetic jet has many advantages over the other AFC method. It does not require an additional air supply system or complex moving parts and therefore it is easy to manufacture and small in size. Moreover, it requires small power to operate while generating a suitable amount of momentum for flow control applications. It is known as a quite effective means of separation control in many flow conditions [10], and there have been many researches to apply synthetic jet on aerodynamic applications including static and dynamic stall control of airfoils, jet vectoring, mixing enhancement, and thermal management [11-15].

A generic synthetic jet is generated by oscillating diaphragm enclosed by immovable walls and one or more orifices (see Fig. 1.5). As the diaphragm moves up and down hundreds of times per second in a periodical motion, the surrounding fluids are suck into the cavity and then expelled to a direction of

the orifice. Although the mechanism is fairly simple, extremely fast cycling requires high-level engineering to produce a device that will last in industrial applications.

Synthetic jet flow can be developed in a number of ways, such as with an electromagnetic driver (e.g. plasma actuator), a flexible diaphragm (e.g. electro-active polymer, ionic polymer, ferromagnetic shape memory alloy and piezoelectric actuator, or even a mechanical driver such as a piston and linear motor [16-22]. In this investigation, piezoelectric actuator was used to drive the oscillating diaphragm. Piezoelectric actuator uses small amount of electric power and small in size with fast response.

Depending on the relative arrangement of the orifice with respect to the oscillating diaphragm, synthetic jet actuator can be categorized into two types [23]. The first is ‘parallel’ synthetic jet actuator in which the orifice is paralleled to the oscillating diaphragm (Fig. 1.6a), and the second is ‘perpendicular’ synthetic jet actuator in which the orifice is located perpendicular to the oscillating diaphragm (Fig. 1.6b). Parallel synthetic jet actuator generates larger jet velocity than perpendicular synthetic jet actuator. But the parallel synthetic jet actuator is hard to satisfy the optimized spacing ratio of actuator spanwise spacing-to-orifice diameter (λ) for separation control established from experiments with arrays of vane vortex generators and fluidic jets, $5 \leq \lambda \leq 20$ [24-26].

The performance of synthetic jet actuator can be indicated by the jet velocity and it is affected by the geometry of actuator and driving signal. The geometry of axisymmetric synthetic jet actuator can be defined by orifice length (h_o), cavity depth (h_c) and diameter of orifice (d_o) and cavity (d_c). And

the driving signal can be defined by its waveform, peak velocity and frequency (f).

1.3 Previous Researches

1.3.1 Synthetic Jet Flow

Smith and Glezer [7] studied the synthetic jet formation and evolution from a rectangular slot. Schlieren imaging and velocity measurements using hot wire anemometer were used to visualize and describe the flow features. They also compared this jet with a conventional two-dimensional jet and found that a synthetic jet entrains more fluid from the surrounding; synthetic jet however loses momentum more rapidly as compared to a continuous jet. Cater and Soria [27] used water as the working fluid instead of air. A piston cylinder assembly was used as the actuator, with a circular orifice on the opposite wall. Using flow visualization images, they categorized the observed flow patterns based on Reynolds number (Re) and Strouhal number (St). By using dimensional analysis, experiments as well as numerical simulations, Utturkar *et al.* [28] proposed jet formation criteria for relatively thick orifice plates (width to hydraulic diameter ratio greater than two) based on Reynolds and Stokes numbers. Holman *et al.* [29] provide the jet formation criterion for orifices of different shapes. Agrawal and Verma [30] have provided a similarity analysis of flow in the far field.

1.3.2 Applying Synthetic Jet on Automobile

Looking at the existing literature, attempts to control the automotive rear wake using a synthetic jet were made for a simplified model by Ahmed *et al.* [31]. They aimed to control the spanwise separation, and the jet emanated from the roof end edge (the junction between the roof and the slanted surface). Leclerc *et al.* [32] performed two-dimensional numerical simulations using the lattice Boltzmann method for a slant angle of 25° . Varying the jet momentum coefficient as well as the jet driving frequency, the aerodynamic drag was decreased in most cases. Brunn and Nitsche [33] performed two-dimensional water channel tests for a slant angle of 35° . Their experiments were performed according to the jet driving frequency, and the drag was decreased in a wide range of jet driving frequencies. As a subsequent investigation, Brunn *et al.* [34] conducted water channel tests for a three-dimensional Ahmed body which was slanted by 35° . As the synthetic jet was activated, the reverse flow region was significantly reduced. These studies showed that the aerodynamic drag of a bluff body can be reduced by a synthetic jet. However, the test conditions were limited to the basic operating parameters of the synthetic jet actuator, which were the jet momentum coefficient and the jet driving coefficient.

1.4 Dissertation Objective and Outline

The purpose of this study is to reduce the aerodynamic drag coefficient of an automobile by synthetic jet as means of an active flow control method. As a preliminary research, parametric study on actuator geometry and driving signal of a synthetic jet actuator was performed and the optimization procedure was followed. And then, the effect of synthetic jet actuation on the aerodynamic drag of a simplified car body is extensively evaluated for various operating conditions of synthetic jet. The Ahmed reference model was used for the wind tunnel test, and the synthetic jet was applied in a form of an array.

The present thesis is organized as follows. The experimental setup and methods for this study are presented in Chapter 2. Chapter 3 shows the parametric study of the synthetic jet actuator. Chapter 4 shows the experimental results for applying synthetic jet on the Ahmed reference model. Finally, the conclusions were made in Chapter 5.

Table 1.1 Regulation on automobile fuel efficiency and CO₂ emission [2]

Period	Standardization
By 2011	Engine displacement below 1,600 cc : Fuel efficiency over 12.4 km/l (CO ₂ Emission : 193.0 g/km)
	Engine displacement above 1,600 cc : Fuel efficiency over 9.6 km/l (CO ₂ Emission : 249.3 g/km)
From 2012	Fuel efficiency over 17 km/l or CO ₂ emission below 140 g/km

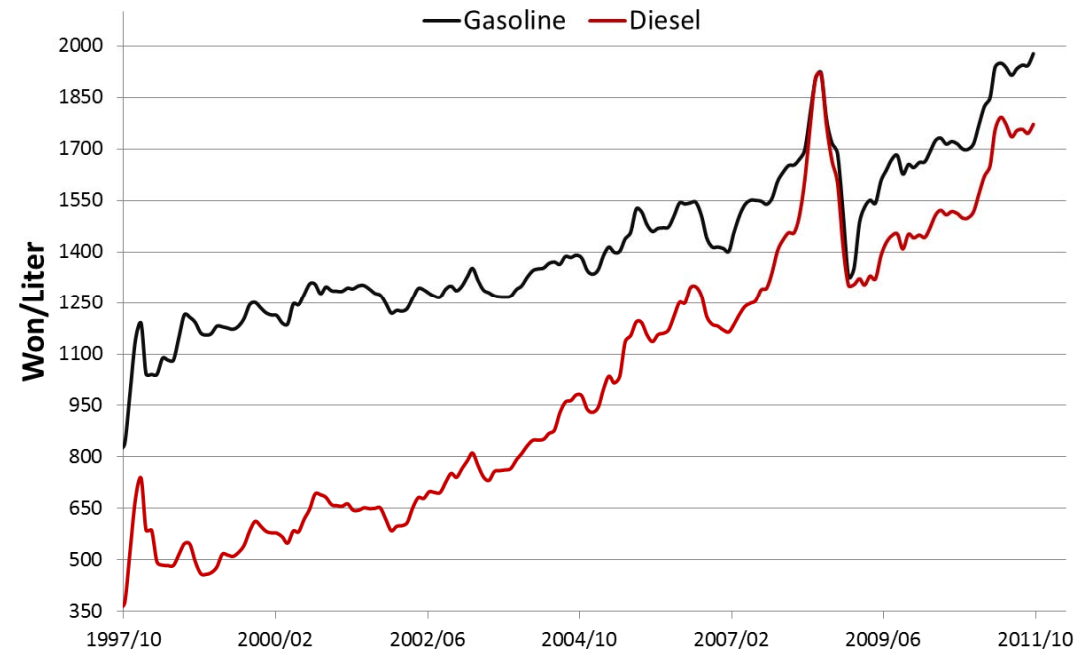
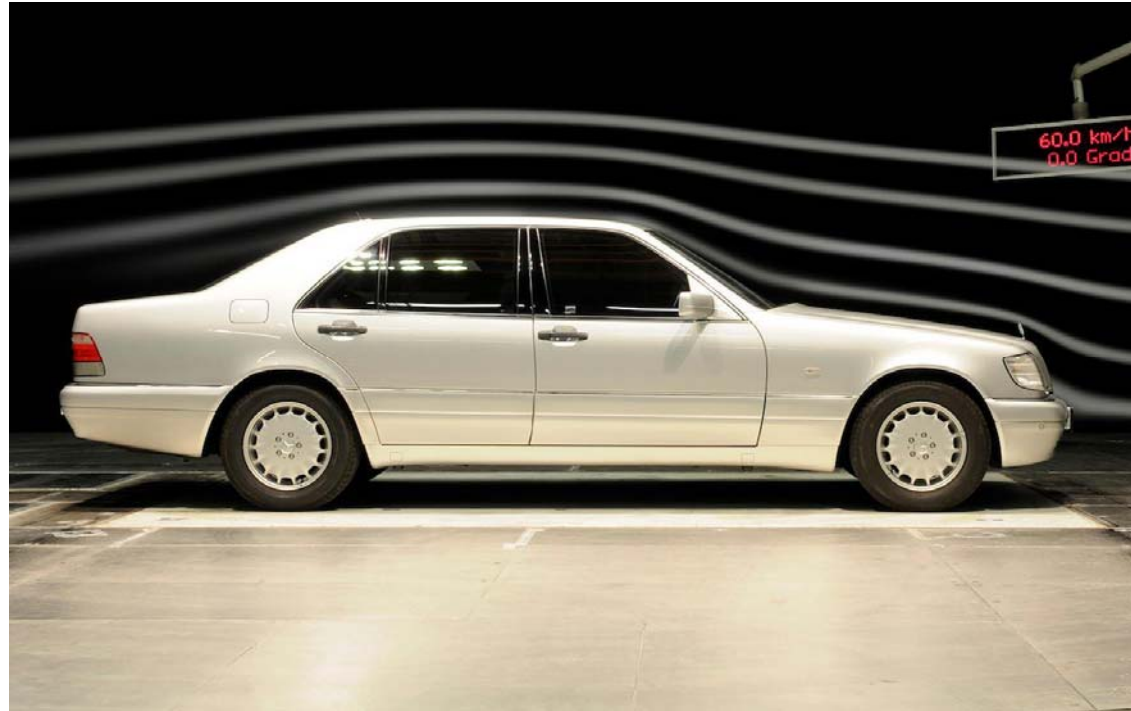


Fig. 1.1 Oil price in South Korea from 1997 to 2011 [1]



**Fig. 1.2 Streamlines in the longitudinal midsection of a Mercedes-Benz S-Class W140 series
(Photograph courtesy of Mercedes-Benz)**

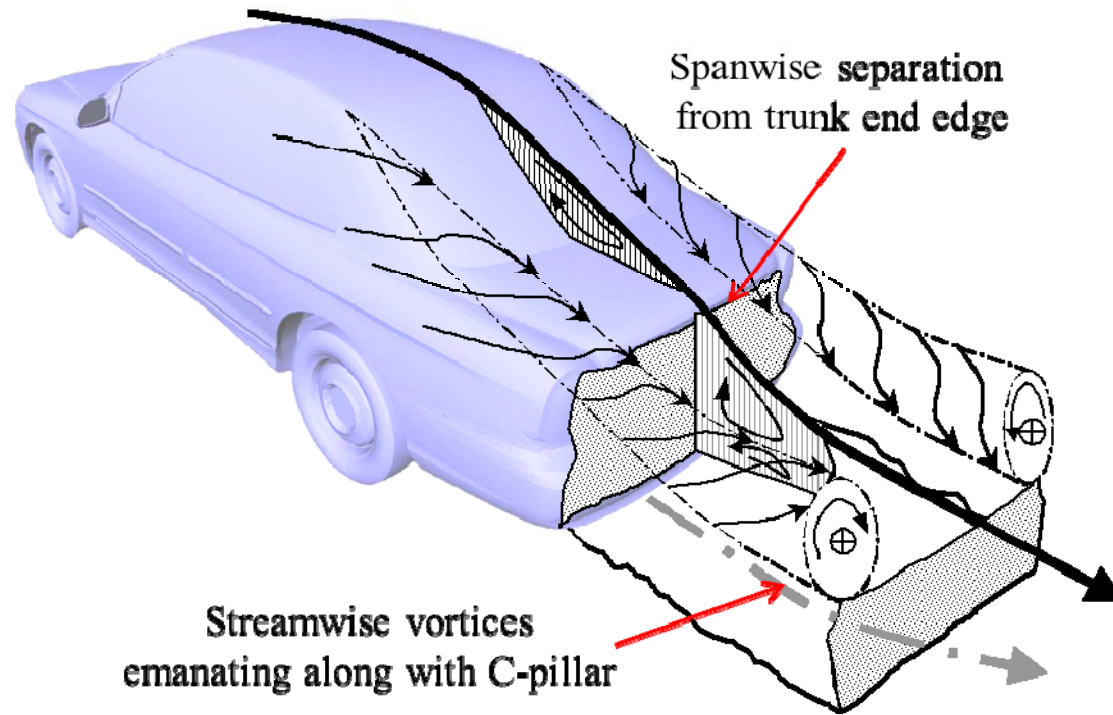
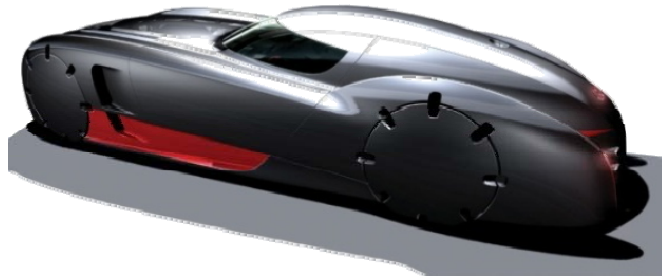


Fig. 1.3 Schematic of flow past a passenger car [5]



(a) Streamlined body



(b) Angulated trunk shape



(c) Trunk kick-up

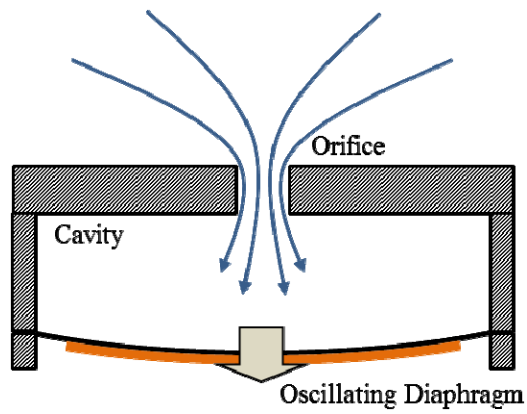


(d) Vortex generator

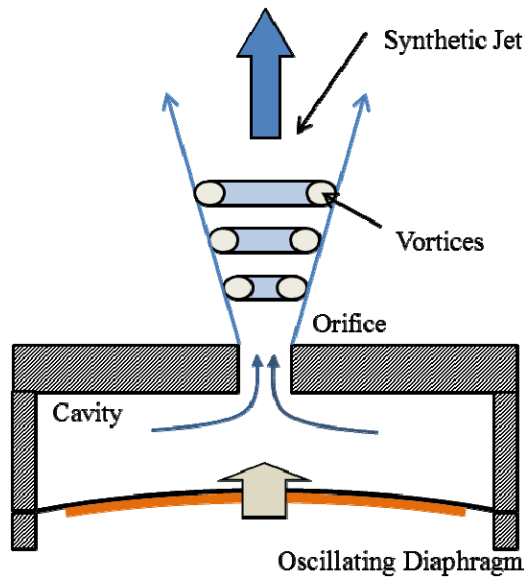


(e) Rear spoiler

Fig. 1.4 Examples of passive flow control method

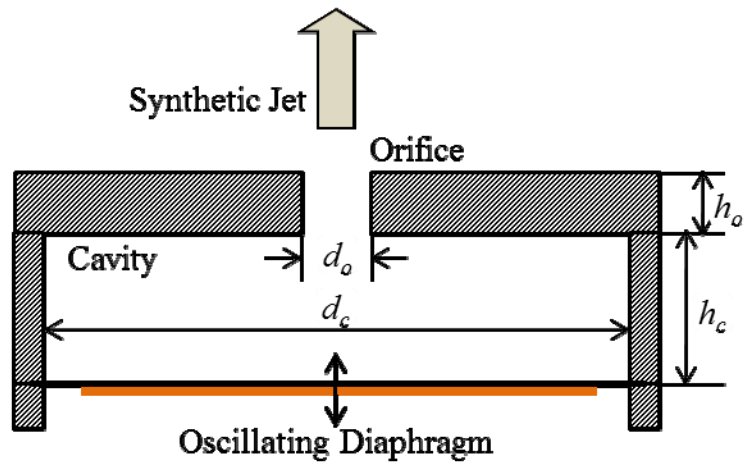


a) Suction phase

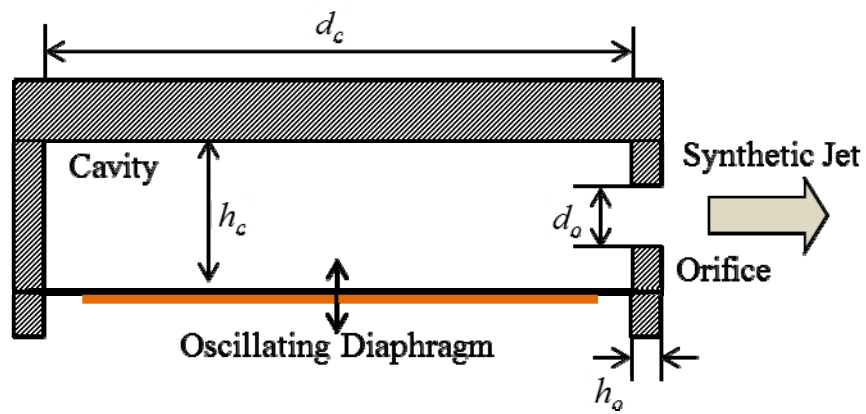


b) Blowing phase

Fig. 1.5 Schematic of synthetic jet actuator



a) Parallel type synthetic jet actuator



b) Opposite type synthetic jet actuator

Fig. 1.6 Two types of synthetic jet actuator

Chapter 2. Description of Experiment

2.1 Wind Tunnel and Experimental Model

The experiments were conducted in a closed-type subsonic wind tunnel in School of Mechanical and Aerospace Engineering at Seoul National University. The dimensions of the test section are 0.95 *m* (height) × 1.34 *m* (width) × 2.44 *m* (length), and the maximum wind tunnel speed is about 75 *m/s* with a turbulent intensity being less than 0.3%. All experiments were performed at a wind tunnel speed of 20 *m/s*. The corresponding Reynolds number is $Re_l = 4.29 \times 10^5$, which is defined as follows:

$$Re_l = \frac{\rho U_0 l}{\mu} \quad (2.1)$$

Here, ρ is the density of the test section, U_0 is the wind tunnel speed, l is the length of the model and μ is the dynamic viscosity of the test section.

In this study, the Ahmed reference model was chosen for the experiments. Fig. 2.1 shows the geometry of Ahmed reference model in original size. The Ahmed body is a typical reference model for an automobile in which numerous complex flows occur in spite of its simple shape [31, 36-38]. The aerodynamic drag of an Ahmed body is largely comprised by the pressure drag (75~85%), which is significantly affected by the flow behind the body. Dominant aerodynamic phenomena around rear body of the Ahmed model are the spanwise separation from the roof end edge and the streamwise horse-shoe

vortices emanating along the slanted side edges (see Fig. 2.2). The structure of rear wake flow is highly dependent on the rear slant angle (θ_s), as is the aerodynamic drag. Fig. 2.3 shows the aerodynamic drag coefficient (C_D) of an Ahmed body according to the slant angle. C_W denotes the total aerodynamic drag. Ahmed *et al.* [31] evaluated contributions to the pressure drag from front surface (C_K^*), slant rear surface (C_B^*), and vertical base surface (C_S^*). And C_R^* denotes skin friction drag. There is a critical slant angle, which is $\theta_{s,crit.} = 30^\circ$. At a low slant angle lower than the critical angle, the wake flow is fully three-dimensional because streamwise vortices exist. The streamwise vortices are created from the slanted side edge. In this region of the slant angle, the aerodynamic drag increases as the streamwise vortices become stronger. When exceeding the critical angle, the streamwise vortices vanish and the two-dimensional spanwise rear separation from the roof end edge dominates the wake region. The aerodynamic drag undergoes dropdown. During this process, there is a large difference in the flow patterns before and after the critical slant angle. Therefore, two slant angles of Ahmed body configurations were chosen for this study, which is $\theta_s = 25^\circ$ and 35° . Geometrically, it can be said that 25° and 35° slanted Ahmed model represent a sedan and a hatchback automobile, respectively. Therefore, flow control strategy for both types of car can be established by present results.

2.2 Measurement and Flow Visualization

Measured physical properties in this study are velocity of wind tunnel free stream and synthetic jet flow, static pressure at rear surface and total aerodynamic drag of Ahmed reference model. And the rear wake flow of Ahmed body was visualized using tuft method.

- **Velocity measurement**

A pitot-static tube was used to measure the free stream velocity of the wind tunnel. The pitot-static tube is the most common device for determining the stream velocity because it is easy to install with accurate measurement. The pitot-static tube that has a total orifice and a static orifice senses the total pressure and the static pressure. When from the two orifices are connected to a pressure transducer, the pressure differential can be approximately considered as dynamic pressure ($1/2\rho V^2$) of Bernoulli's equation in the subsonic flow, from which the stream velocity could be calculated [39]. In the present experiments, the free stream velocity in the wind tunnel was obtained using a pitot-static tube connected to different pressure transducer which is MKS Baraton 220 Model having $\pm 100 \text{ mmHg}$ of full scale, 0.01% resolution of full scale reading, and an accuracy of 0.15% reading.

Hot wire was used to measure the jet velocity of synthetic jet actuator. Hot wire is usually used for the measurement requiring fast response in turbulence flow as well as in laminar flow. Hot wire anemometers use a very fine wire (order of several micrometers) electrically heated up to some temperature above the ambient. Air flowing past the wire has a cooling effect on the wire.

As the electrical resistance of most metals is dependent upon the temperature of the metal (tungsten is a popular), a relationship can be obtained between the resistance of the wire and the flow speed [40]. In this measurement, CTA (constant-temperature anemometer) device was used. The voltage output from the anemometers is the result of some sort of circuit within the device trying to maintain the temperature constant. In subsonic flows where the density is high and the flow temperature is low and constant, the problem of heat transfer through the supports and radiation effects can be ignored, and the wire's response is basically a function of velocity alone. Under these conditions, using appropriate calibration and measurement of the voltage across the bridge, both mean and turbulent velocities are usually obtained by using King's Law [41]. The equation is as follows.

$$E^2 = A + BV^n \quad (2.5)$$

, where E is a voltage of CTA, V is a velocity and A , B , and n are constants to be determined during the calibration procedure. In this study, synthetic jet velocity was measured using the hot wire that is a single normal type with 5 micrometer tungsten under a constant temperature mode using KANOMAX 1011 model. A static calibration of the hot wire based on Kings' Law is carried out by placing the hot wire measurement, and the calibration has been performed in every experiment so that the maximum error of hot wire should be less than 5% over the whole range of velocity considered. The hot wire probe is place into a specific position by a 3-axis auto traverse system with 0.1 mm accuracy in movement.

- **Force measurement**

Total aerodynamic drag of Ahmed body was instrumented by load cell to reveal the effect of synthetic jet actuation. A load cell is a transducer that is used to convert a force into electrical signal [42]. This conversion is indirect and happens in two stages. Through a mechanical arrangement, the force being sensed deforms a strain gauge. The strain gauge measures the deformation (strain) as an electrical signal, because the strain changes the effective electrical resistance of the wire. A load cell usually consists of four strain gauges in a Wheatstone bridge configuration. Load cells of one strain gauge (quarter bridge) or two strain gauges (half bridge) are also available [43]. The electrical signal output is typically in the order of a few millivolts and requires amplification by an instrumentation amplifier before it can be used. The output of the transducer can be scaled to calculate the force applied to the transducer. In this investigation, the total aerodynamic drag was instrumented by a single-point high-definition one-axis load cell, the OBU 1004K from Bongsin Co. From specification of manufacturing company, the aerodynamic drag for this wind tunnel model may be measured within an accuracy level of 0.2%. The load cell was located at the center of the bottom surface.

- **Pressure measurement**

The mean surface pressure was measured through static pressure taps distributed over surface of interest. Each pressure was connected to a pressure transducer, which are 16 channel pressure scanners (Net Scanner 9116 by Measurement Specialties) and 16 pressure transducers (SP007 by Delta

Metrics). Net Scanner 9116 is available with full scale pressure ranges from 2.5 to 6.895 *kPa* with accuracy of $\pm 0.05\%$. And the range of SP007 is from 0 to 6.895 *kPa* with accuracy of $\pm 0.25\%$. When the surface pressure is measured using a small diameter tube, the propagation of pressure in the tube must be considered. The pressure propagation from pressure tap of the surface to the pressure transducer is supposed to have a time delay depending on the diameter and the length of the tube [44-45]. The preliminary test on the pressure propagation was conducted and found that the time constant is less than 1 second. This time delay was considered in pressure measurement.

- **Flow visualization: tuft method**

The flow visualization technique is an efficient experimental method for observing the flow structure or judging the separated flow. In this study, a tuft method is adapted to visualize the flow. The tuft method is one of the earliest techniques of flow visualization. Basically, tufts are point indicator of the focal flow direction. This is often used to distinguish between attached and separated flow and each tufts can depict the flow status at only one location.

In the present study, the rear wake flows are visualized using tufts to reveal the change in the rear wake flow caused by the actuation of the synthetic jet,. Three tufts are suspended above the roof end edge on the symmetry plane by a thin nylon wire.

2.3 Data Acquisition

Data Acquisition (DAQ) is a sampling process of analog signal and conversion of the samples into digital numeric values that can be manipulated by a computer. The DAQ system which was used for these experiments is based IBM PC equipped data acquisition boards. All processes of controlling output signal and acquiring input data were performed by LABVIEW software. All data were handled and calculated in this program simultaneously and automatically.

The DAQ boards are NI USB-6221 and NI PCI-6281 of National Instruments Inc. Both DAQ boards are connected to the IBM PC for acquiring physical data using LabView program. The NI USB-6221 multifunction board has 16 analog inputs (16 bit, 250 *kS/s*), two analog outputs (16 bit, 833 *kS/s*), and 24 digital I/O. The NI PCI-6281 board has two analog outputs (16 bit, 2.8 *MS/s*), and 24 digital I/O..

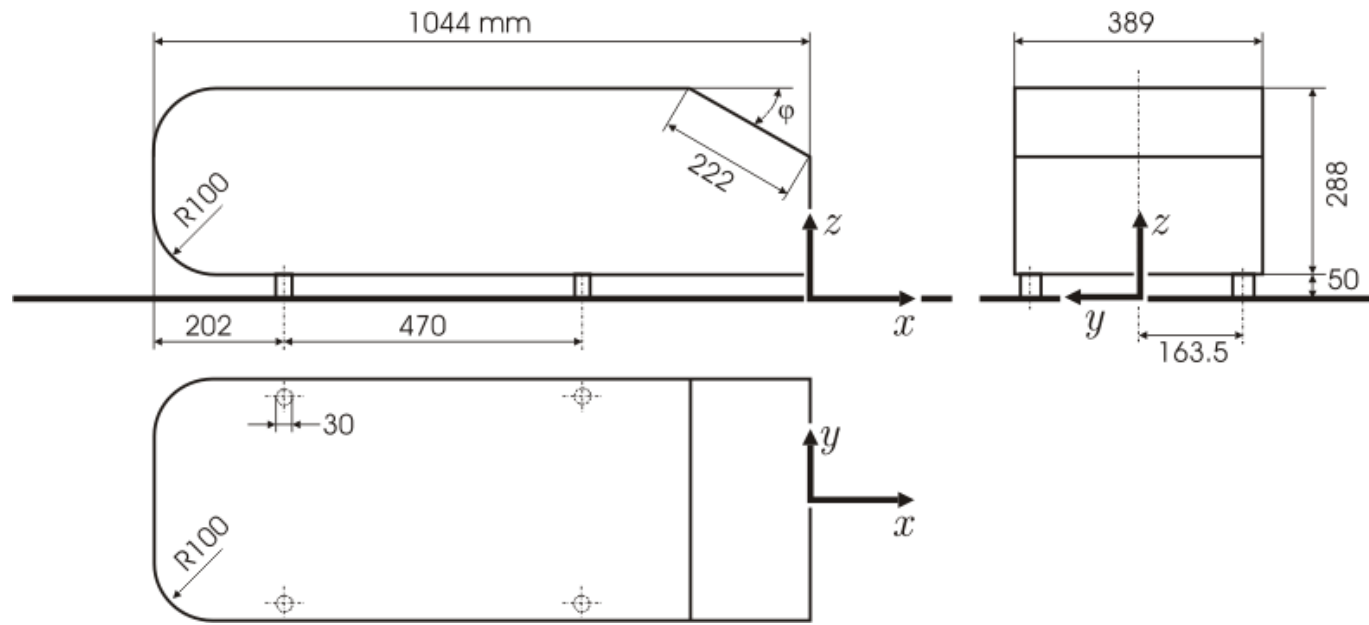


Fig. 2.1 Ahmed reference model configuration in original size (dimensions given in *mm*) [35]

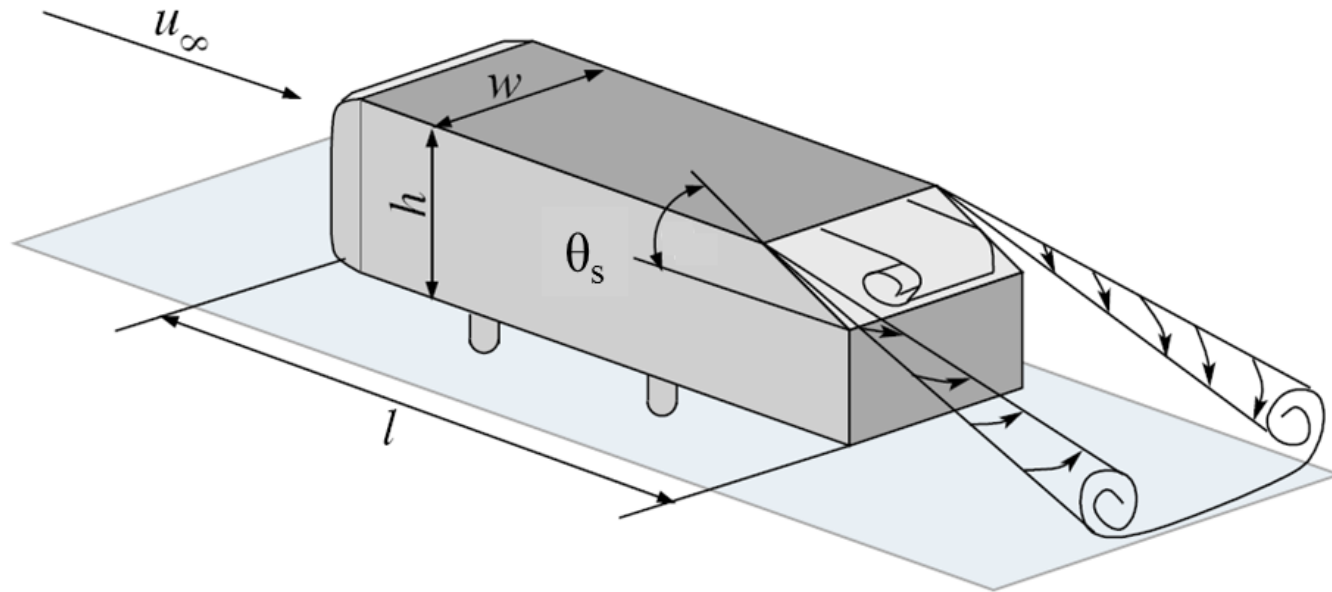


Fig. 2.2 Schematic of flow over an Ahmed reference model [19]

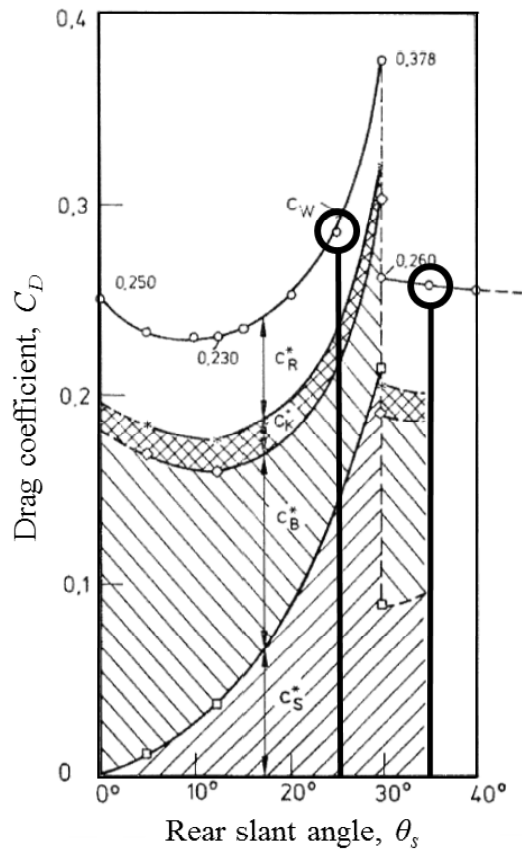
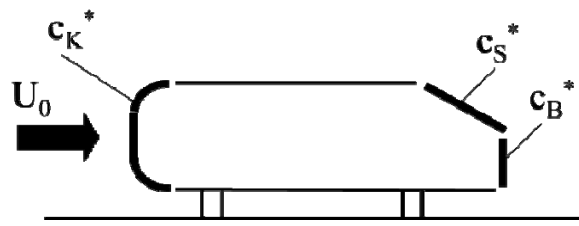


Fig. 2.3 Aerodynamic drag coefficient of Ahmed body according to the rear slant angle [31]

Chapter 3. Design of Synthetic Jet Actuator

Over the years, research has shown that behavior of synthetic jet actuator is dependent on its geometry and driving condition of diaphragm; hence, the focus of this work. In this study, the jet velocity of the parallel synthetic jet actuator is studied under factors related to the actuator geometry and driving signal. The overall factors considered are the orifice length, cavity depth, and driving frequency. Using the average of maximum jet velocity of blowing phase as a response variable, these factors are individually studied. And then, the meta model was constructed by Artificial Neural Network method (ANN) and the optimal design was performed by using the gradient based optimization algorithm.

3.1 Experimental Setup

3.1.1 Perpendicular Synthetic Jet Actuator

For the purpose of this study, the synthetic jet actuator was consisted by three ABS resin plates, two urethane bands, and one piezoelectric actuator. Fig. 3.1 shows components of the synthetic jet actuator. Three 88 *mm* by 88 *mm* ABS resin plates form the orifice and the immovable walls of the cavity. From the left of Fig. 3.1, the first component provides an orifice of the synthetic jet

actuator. Hole in the center becomes the orifice of the synthetic jet actuator. The orifice is circular and the diameter is fixed to 2 mm . And next, the cavity plate is depicted. This ABS resin plate has a 65 mm circular aperture in the center, and a 5 mm wide and 1 mm deep groove is machined along the perimeter of the aperture to insert the urethane band. This circular aperture becomes a cavity of the synthetic jet actuator. At the far right of Fig. 3.1, the base plate is depicted. It has also a large hole in the center and groove for urethane band and has two ports for the electrical leads of the piezoelectric actuator. The piezoelectric actuator was located between the cavity plate and the base plate. To prevent failure of the piezoelectric actuator during the tests, a THUNDER™ actuator was employed, which produces comparatively high block force with a large amount of displacement. The THUNDER™ actuator was developed by NASA Langley Research Center and produced by Face(R) Co. The base plate of the THUNDER™ actuator is stainless steel, 68.5 mm in diameter. And the PZT element is a soft PZT type 5A, 63.5 mm in diameter. Two urethane bands were inserted between the piezoelectric actuator to maximize the displacement of the piezoelectric actuator by providing cushioning while maintaining the seal. The urethane band fit to the groove in the cavity and base plate. Eight screws with washers are used to clamp the components. Equal torque of 0.42 Nm is applied on each screw using a torque screwdriver to ensure constant pressure along the perimeter of the actuator. Figure 3.2 shows the final assembly of the synthetic jet actuator.

3.1.2 Measurement System

Figure 3.3 shows schematic of the jet velocity measurement system. The driving signal was applied varying frequencies for each synthetic jet actuator. This signal is applied using a signal generator provided by the DAQ board (NI PCI-6281), connected to an HVPZT amplifier (E-481). As the synthetic jet flow generates, the jet velocity was measured by hot wire anemometer. The location of the hot wire probe was determined by three-axis traverse. The voltage signals of the jet velocity were analyzed by CTA model 1011, and it was recorded using the DAQ system. The amplitude and frequency of the applied signal were kept below their allowable maximums in order to prevent electrical and mechanical failure of the diaphragms. A sinusoidal waveform was used to drive a piezoelectric actuator, which is known to provide the best waveform for a synthetic jet actuator [46]. The velocity is measured in quiescent air at a fixed distance of 2 mm in the vertical direction for each actuator during 2 seconds. And the synthetic jet actuator and how wire probe was enclosed by the control volume box to assure the quiescent flow condition, which is 700 mm × 700 mm × 700 mm in size (Fig. 3.4).

3.1.3 Experimental Parameters

Performance of a synthetic jet actuator is dependent on the parameters related to the actuator geometry and driving signal [47-52]. The geometry of parallel type of synthetic jet actuator can be defined by its orifice diameter (d),

orifice length (l), cavity diameter (D) and cavity depth (H) (Fig. 1.6a). And the driving signal is defined by waveform, amplitude, and frequency. In this study, the effects of orifice length, cavity depth, and driving frequency on the jet velocity were studied. Parameters varied in this study are summarized in Table 3.1. To study the effects of frequency on the jet, the velocity is measured at 38 frequencies from 30 Hz to 400 Hz in step of 10 Hz . These experiments are conducted on nine synthetic jet actuator configurations. The differences in the actuators are the cavity depth and the orifice length. They were changed from 5 mm to 15 mm .

3.2 Parametric Study on Parallel Synthetic Jet Actuator

A typical velocity curve formed with a sine waveform is shown in Fig. 3.5. Two peaks are observed, with the second one smaller in magnitude. The first peak (larger one) follows the negative peak of the input signal and the second peak (smaller one) follows the positive peak. The larger peak is believed to occur during the blowing cycle, while the smaller peak is believed to occur during the suction cycle. Previous studies on the synthetic jet flow fields have indicated that during the suction cycle the flow reenters the cavity from the sides of the orifice [7]. Thus the second peak may be due to the nonparallel direction of the flow, relative to the hotwire, entering the cavity. In this research, the maximum velocity of blowing phase is selected as a response variable.

3.2.1 Effect of Jet Driving Frequency on Jet Velocity

From an analysis of Gallas *et al.* [52], there exist two resonance frequencies, the cavity resonance frequency and the mechanical resonance frequency of diaphragm. The cavity resonance frequency (f_c) is given by

$$f_H = \left(\frac{c}{2\pi}\right) \left(\frac{2\pi r_o^2}{V_c \times h_o}\right)^{0.5} \quad (3.1)$$

where c is the speed of sound, h_o is the orifice length, r_o is the radius of

orifice, and V_c is the volume of the cavity. Fig. 3.6 shows the maximum jet velocity according to the jet driving frequency. The jet driving frequency was varied from 100 *Hz* to 950 *Hz* in step of 50 *Hz*. Geometry of the synthetic jet actuator used for this experiment was 2 *mm* in orifice diameter, 5*mm* in orifice length, 65 *mm* in cavity diameter, and 5 *mm* in cavity depth. From the results, the jet velocity shows two peaks around $f= 250\sim 300$ *Hz* and 700~800 *Hz*. And the calculated cavity resonance frequency from eq. (3.1) is 275 *Hz*. Therefore peak at low frequency seems as the cavity resonance and the other is mechanical resonance of the diaphragm. Because actuation near the mechanical resonance may cause the destruction of the piezoelectric actuator, the former resonance is more important in the present set of experiments and need to be used properly to increase the jet velocity. Furthermore, because the jet velocity was gradually changed near the cavity resonance frequency, large jet velocity can be obtained at relatively wide frequency range, while the change in jet velocity due to the mechanical resonance was so steep and occurred in a narrow range of jet driving frequency.

3.2.2 Effect of Actuator Geometry on Jet Velocity

Figs. 3.7~12 show the jet velocity according to the jet driving frequency for each orifice length and cavity depth. At low frequencies (about 30 ~ 150 *Hz*), jet velocity increases linearly with the driving frequency. The orifice length and cavity depth do not affect the jet velocity significantly at this frequencies. And then, a single resonance frequency was observed and the

maximum jet velocity was observed at this frequency which depends on the actuator geometry. In Table 3.2, cavity resonance frequency calculated by Eq. (3.1) and experimental maximum jet velocity and frequency are arranged. The frequency showing maximum jet velocity is between 110 *Hz* and 320 *Hz*, which agrees with the values of cavity resonance frequency calculated from Eq. (3.1) with 10% error except for 5 *mm* of cavity depth. And the maximum jet velocity increases linearly with the cavity resonance frequency by Eq. (3.1). On the other hand, behaviors of jet velocity after the resonance are different according to the actuator geometry. In most cases, jet velocity decreases as exceeding the peak velocity (Fig. 3.11-12). However for a small orifice length (5 *mm*), the jet velocity was not decreased as exceeding the cavity resonance frequency, but rather increased a little (Fig. 3.10). To make it easier to understand this, it was shown three-dimensionally in Fig. 3.13. This is shown by interpolating the data of Fig. 3.7-12.

3.3 Optimal Design of Parallel Synthetic Jet Actuator

From the previous results, it is seen that synthetic jet velocity is significantly influenced by orifice length and cavity depth at some high jet driving frequency. In this chapter, shape optimization was performed with the experimental data. Meta model was constructed using Artificial Neural Network method (ANN), and Optimization was performed using gradient based optimization algorithm.

3.3.1 Design Problem Formulation

The conventional deterministic optimization (DO) generally consists of an objective function $f(x, p)$ and constraints $g(x, p)$, which are given as follows:

$$\begin{aligned} \text{Minimize} \quad & f(x, p) \\ \text{Subject to} \quad & g_i(x, p) \leq 0 \quad I = 1, \Lambda, m \\ & x^L \leq x \leq x^U \end{aligned} \quad (3.2)$$

Jet velocity is the most important factor indicating the performance of piezoelectric synthetic jet actuator. Piezoelectric actuator is small in size and light in weight, therefore using the piezoelectric actuator as a driver of synthetic jet actuator brings many advantages. However the displacement of piezoelectric actuator is so small, only about two to three hundreds of micrometers, that mass flux expelling through the orifice is very small, which

means small momentum capability. Therefore, maximization of the jet velocity is identified as the design objective. And the maximum velocity during blowing phase was selected for response. And the design variables and design space are same with the parameters and ranges of previous parametric study, respectively. Design variables are orifice length, cavity depth and jet driving frequency. Finally, the design problem of this study is given as follows:

$$\begin{aligned}
 & \text{Maximize} && \text{Maximum jet velocity} \\
 & \text{Subject to} && 5 \text{ mm} \leq \text{Orifice length} \leq 15 \text{ mm} \quad (3.3) \\
 & && 5 \text{ mm} \leq \text{Cavity depth} \leq 15 \text{ mm} \\
 & && 30 \text{ Hz} \leq \text{Jet driving frequency} \leq 400 \text{ Hz}
 \end{aligned}$$

3.3.2 Artificial Neural Network

Artificial Neural Network (ANN) was created based on the ideas of how human nervous system transfers and handles the information. It understands the behaviors of output variables by input variables and defines the relationship between the input variables and the output variables in mathematical form. ANN has a good advantage in representing the nonlinear problems of the complex system [53-55]. In the ANN method, data processing unit which is called ‘Neuron’ assemble and judge from the existing state of things in the design optimization problem. Neuron adds external stimuli with multiplying weighting factors, then deliveries the data to the next neuron by a

transfer function. The set of the neurons, which uses same previous data, is defined as ‘layer’ and the whole artificial neural network is constructed by assembly of the layers. Generally, 3-layer artificial neural network is commonly used and comprised of ‘input layer’, ‘hidden layer’, and ‘output layer’.

In order to perform the efficient design optimization, ANN models were used to construct a meta model. The ANN models which are composed of an input layer with three neurons (two geometry variables and one driving frequency), a hidden layer with eight neurons and an output layer with one neurons (maximum jet velocity) are constructed (Fig. 3.14). From ANOVA analysis in Table 3.3, R^2 values are close one and RMS error converges to zero, which means the accuracy of approximation of the ANN model is very high.

3.3.3 Optimization Result

Finally, DOT is adopted to optimize the ANN models. DOT is a design optimization tool developed by Vanderplaats *et al.* [56]. DOT is basically a gradient based optimizer and known to be very robust and efficient compared with other optimizers. Functions optimized by DOT may be linear or nonlinear and maybe very complicated implicit function of the design variables. Three methods are available for the constrained optimization in DOT, and the Fletcher-Reeves method is selected for the optimization process which uses very little computer memory and reliable.

In Table 3.4, the optimization result is summarized below. The jet velocity

was increased as the cavity depth decreases, and converged to 5 *mm* of cavity depth which is the minimum value. On the other hand, overall trend orifice length was same with the cavity depth. However, the maximum jet velocity was occurred at 8.58 *mm* of orifice length rather than at a minimum value. It is because that directionality of the jet due to orifice wall is reduced. If orifice is too short, even the pressure loss due to the orifice wall is decreased. And the optimized jet velocity was emanated at 293.7 *Hz* of jet driving frequency under the influence of cavity resonance. Figs. 3.15-17 show the design space and objective for each two design variables. The left one is 2-D contour of the objective function and the right one is 3-D view of the left one for convenience. In all figures, the optimum points show a good agreement with the results in Table 3.4. In these figures, the rest design variables are set as the optimum values. They show moderately simple characteristics. That is, the design space has one global optimum at each case. Therefore, they seem to be approximated well by the ANN model.

Table 3.1 Experimental parameters for synthetic jet actuator design

Parameter		Range
Orifice	Diameter	<i>2 mm</i>
	Length	<i>5, 10, 15 mm</i>
Cavity	Diameter	<i>65 mm</i>
	Depth	<i>5, 10, 15 mm</i>
Oscillating diaphragm	Frequency	<i>From 30 to 400 Hz (in step of 10 Hz)</i>
Total No. of Experiment : $3 \times 3 \times 38 = 342$ times		

Table 3.2 Cavity resonance frequency and maximum jet velocity for each actuator configuration

Actuator geometry		Cavity resonance frequency Eq.3.1 (Hz) ⁽¹⁾	Experimental data		Error between (1) and (2)
Cavity depth (mm)	Orifice length (mm)		Frequency at max. velocity (Hz) ⁽²⁾	Max. velocity at (2) (m/s)	
5	5	319	290	26.3	10.0
5	10	226	340	22.3	33.7
5	15	184	240	15.3	23.3
10	5	238	260	24.6	8.4
10	10	168	180	18.1	6.4
10	15	138	150	14.5	8.3
15	5	198	200	20.3	0.8
15	10	140	150	15.2	6.5
15	15	114	120	13.1	4.6

Table 3.3 Reliability of ANN model (Analysis of variance)

	R^2	RMS error
Max. jet velocity	0.9994	0.025434

Table 3.4 Optimized parameters of synthetic jet actuator

Objective	Max. jet velocity	<i>27.03 m/s</i>
Design variables	Orifice length	<i>8.58 mm</i>
	Cavity depth	<i>5.00 mm</i>
	Jet driving frequency	<i>293.7 Hz</i>

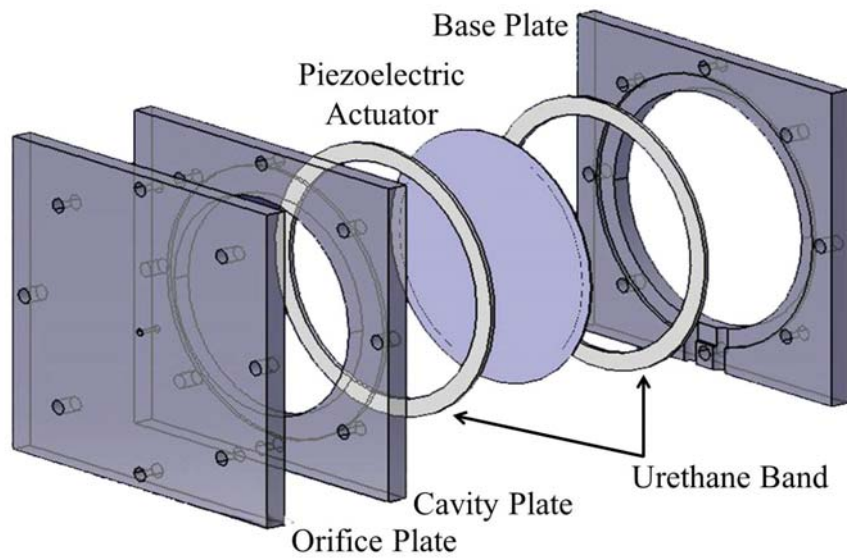
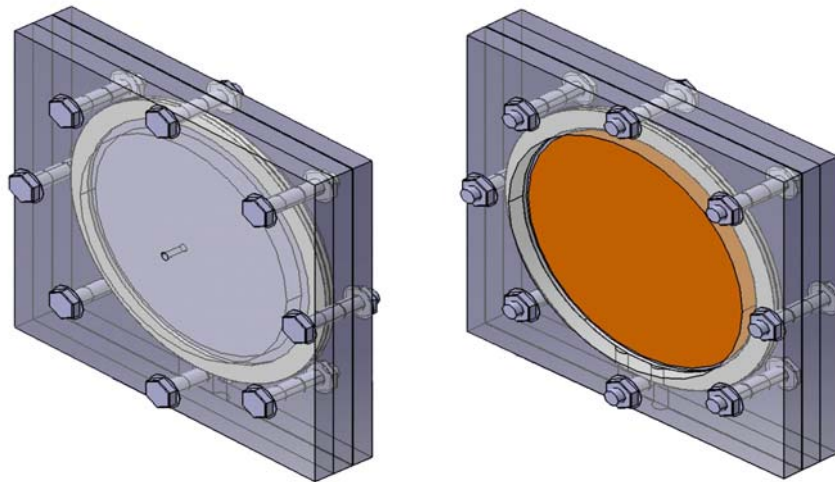


Fig. 3.1 Components of parallel type synthetic jet actuator



(a) Orifice side

(b) Oscillating diaphragm side

Fig. 3.2 Final assembly of parallel type synthetic jet actuator

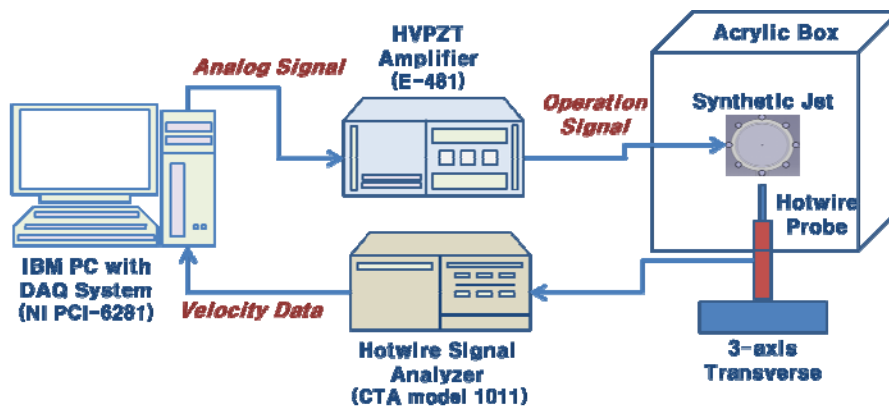


Fig. 3.3 Schematic of jet velocity measurement system



Fig. 3.4 Synthetic jet actuator installed in the control volume box

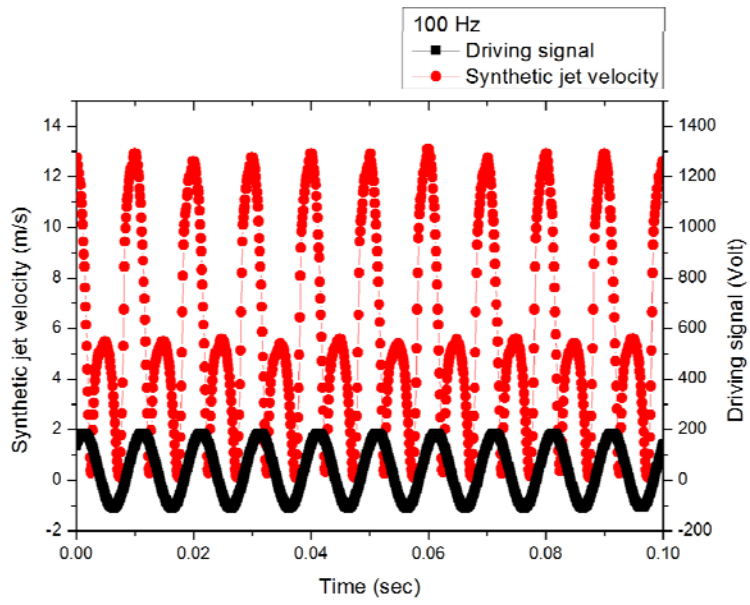


Fig. 3.5 Sample of synthetic jet velocity curve

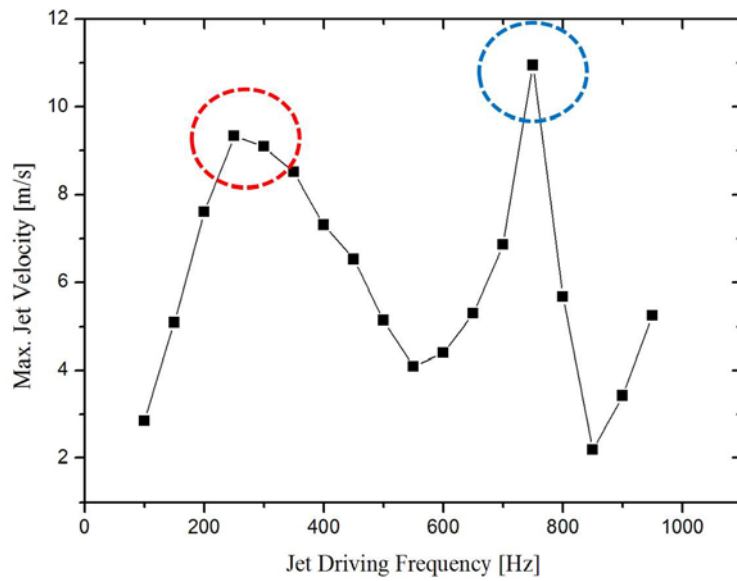


Fig. 3.6 Synthetic jet velocity according to driving frequency

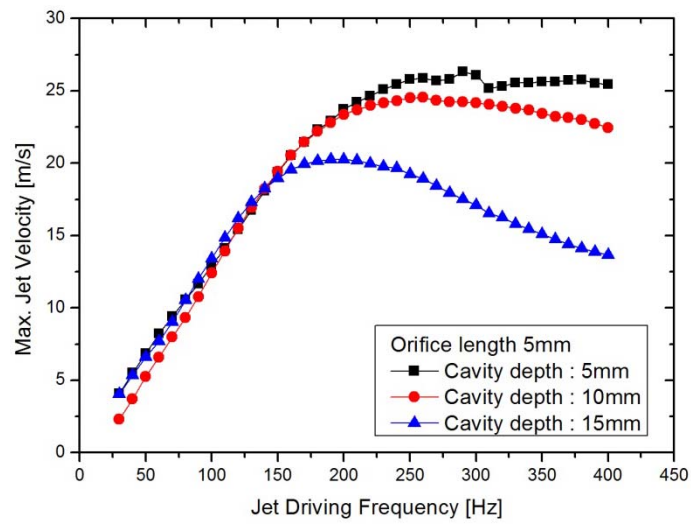


Fig. 3.7 Max. synthetic jet velocity according jet driving frequency at 5 mm of orifice length and 5, 10, 15 mm of cavity depth

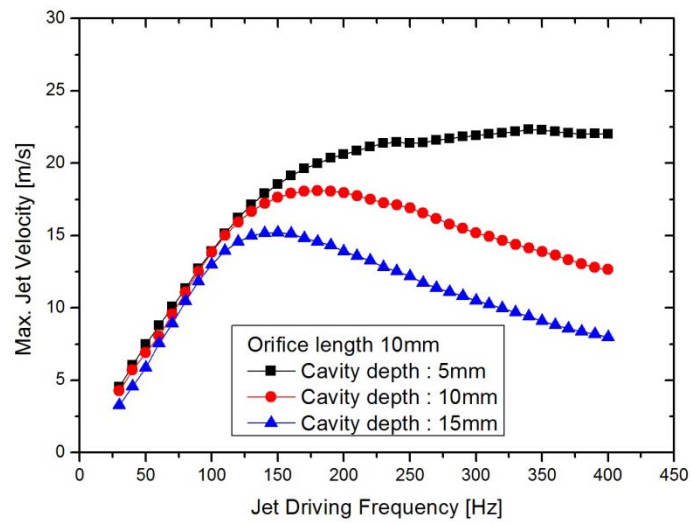


Fig. 3.8 Max. synthetic jet velocity according jet driving frequency at 10 mm of orifice length and 5, 10, 15 mm of cavity depth

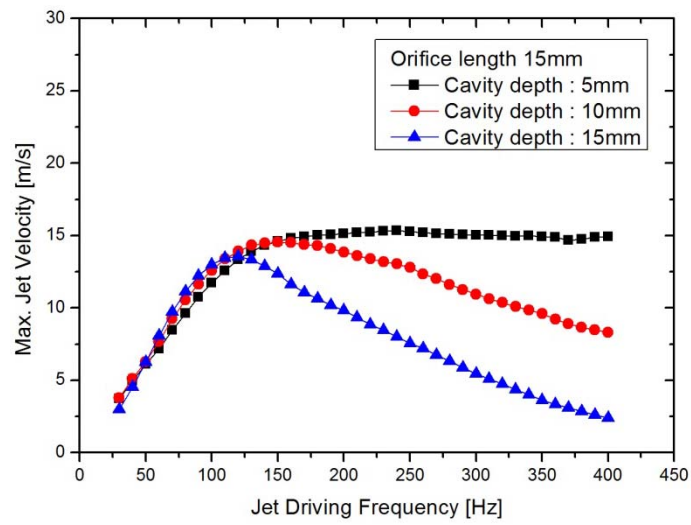


Fig. 3.9 Max. synthetic jet velocity according jet driving frequency at 15 mm of orifice length and 5, 10, 15 mm of cavity depth

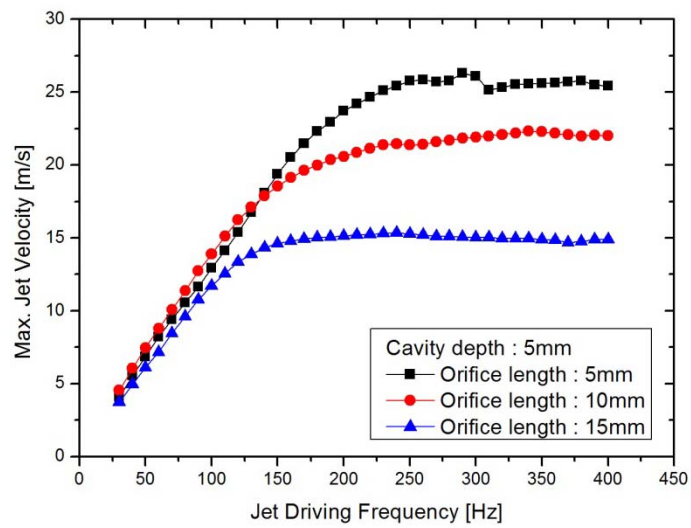


Fig. 3.10 Max. synthetic jet velocity according jet driving frequency at 5, 10, 15 mm of orifice length and 5 mm of cavity depth

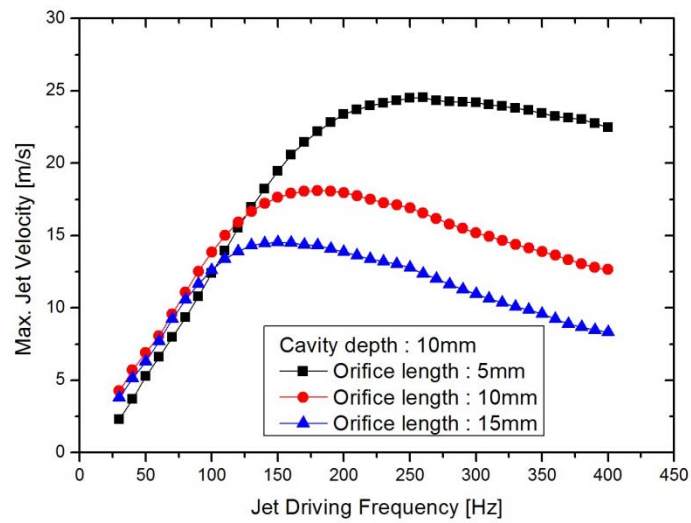


Fig. 3.11 Max. synthetic jet velocity according jet driving frequency at 5, 10, 15 mm of orifice length and 10 mm of cavity depth

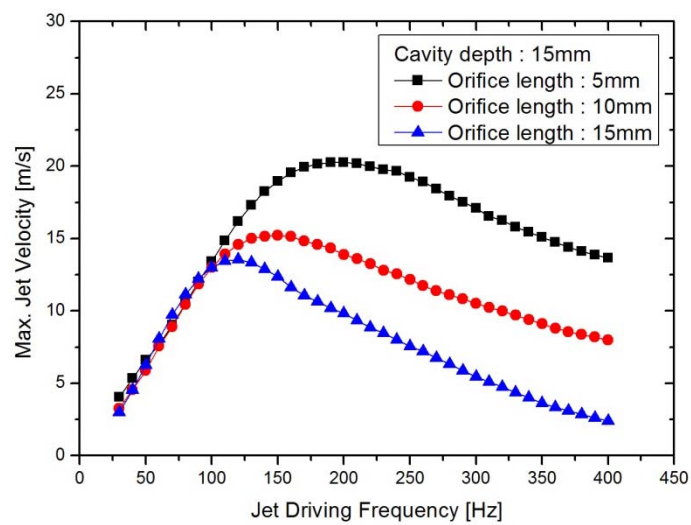


Fig. 3.12 Max. synthetic jet velocity according jet driving frequency at 5, 10, 15 mm of orifice length and 15 mm of cavity depth

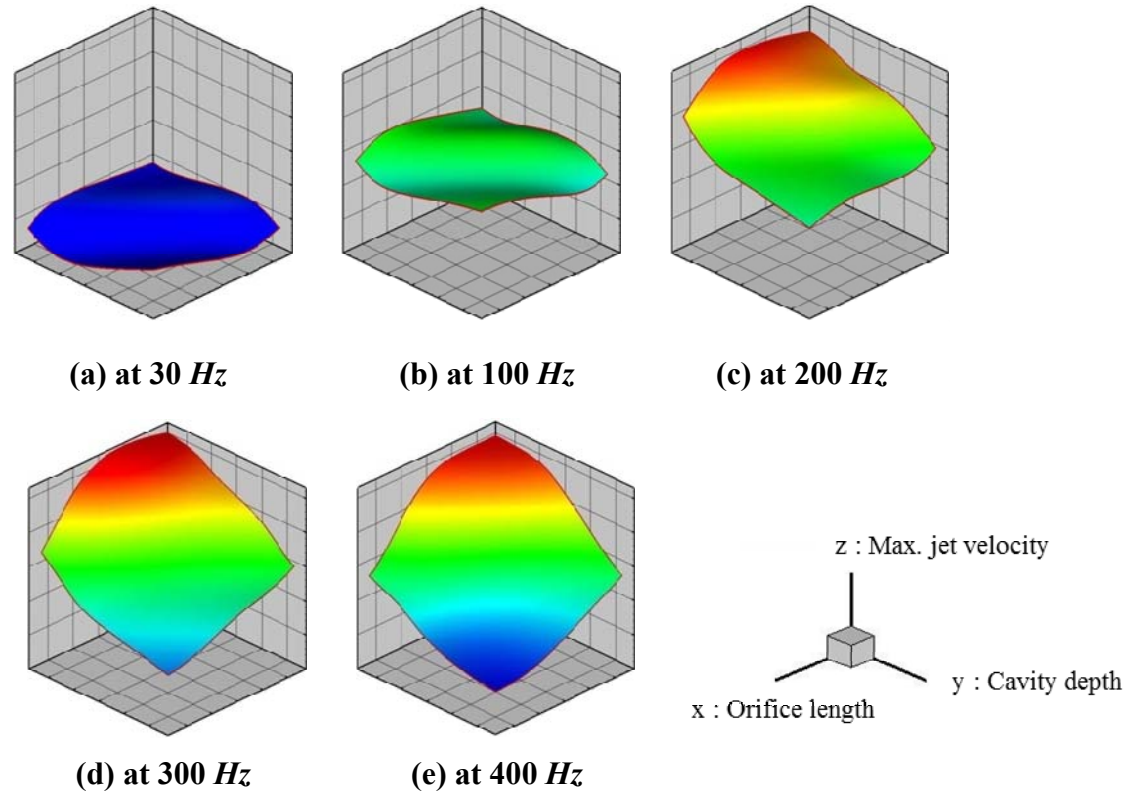


Fig. 3.13 3D contours of max. synthetic jet velocity according to the actuator geometry

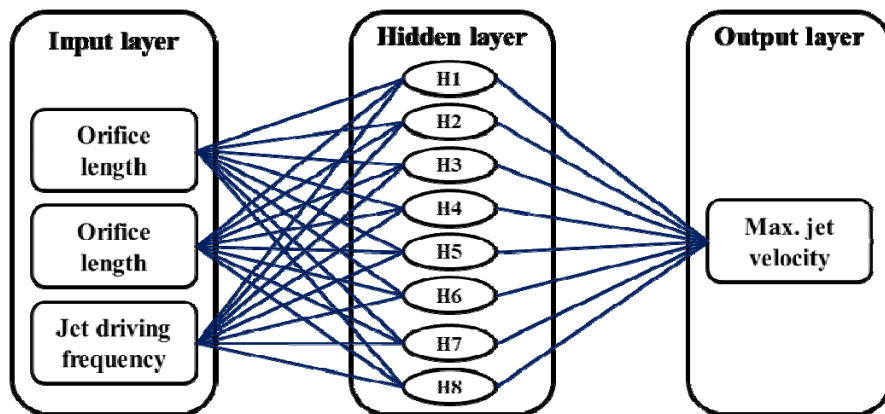


Fig. 3.14 Construction of Artificial Neural Network (ANN) model

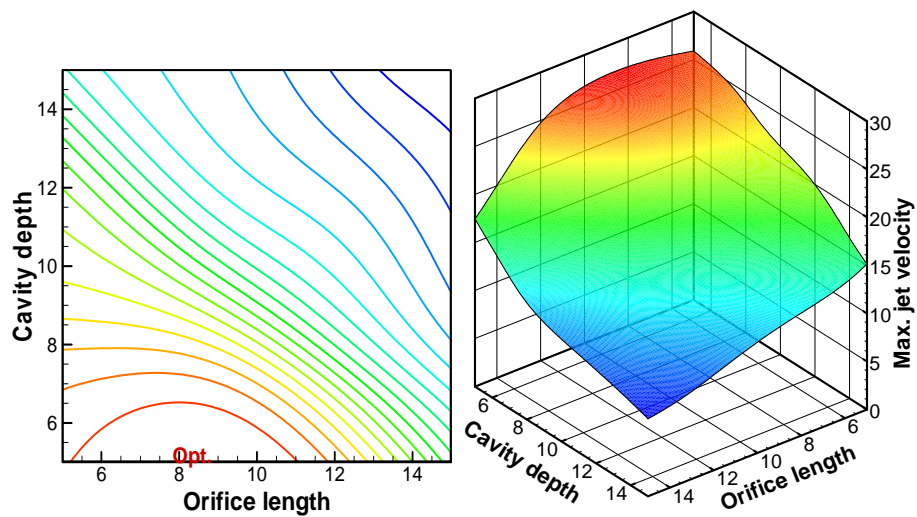


Fig. 3.15 Objective contour according to cavity depth and orifice length

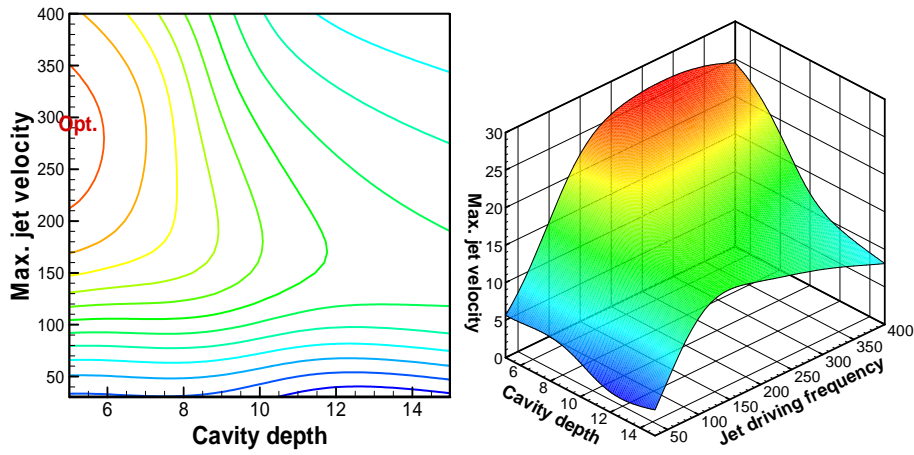


Fig. 3.16 Objective contour according to cavity depth and jet driving frequency

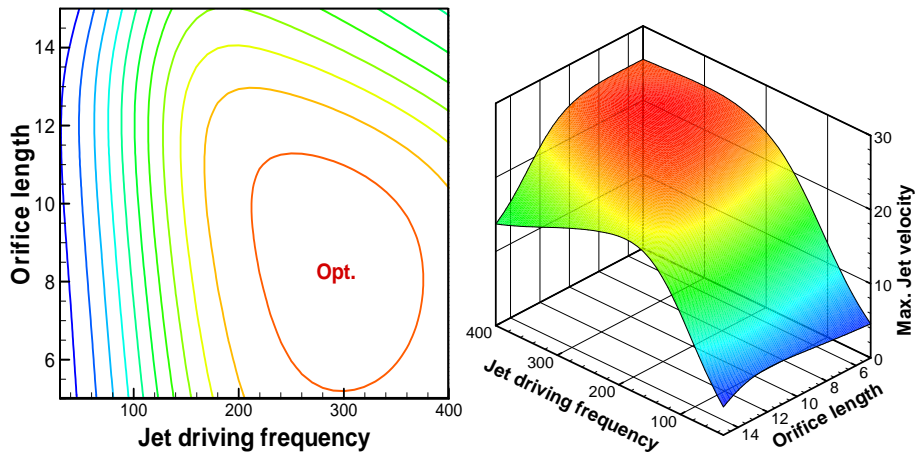


Fig. 3.17 Objective contour according to jet driving frequency and orifice length

Chapter 4. Active Control of Flow over an Ahmed Reference Model using Synthetic Jet

In this study, synthetic jet was employed to control the rear wake flow of the Ahmed body. For two configurations of an Ahmed body (slanted by 25° and 35°) owing different wake topologies [31, 35-38], the synthetic jet is emanated in a form of an array which is consisted by twelve synthetic jet actuators. Jet location, jet direction, jet momentum coefficient, jet driving frequency, and number and position of activated jet within the actuator array were changed to assess the effect of the synthetic jet array. The total aerodynamic drag coefficient was compared in each case. And the changes in the rear wake flows were studied by rear surface pressure and tuft visualization to reveal the mechanism of the change in the aerodynamic drag.

4.1 Experimental Setup

4.1.1 Experimental Model

Fig. 4.1 shows the geometry of the Ahmed body used in the present wind tunnel tests. The test models have two rear slant angles of 25° and 35°, a cross-sectional area of $1.07 \times 10^4 \text{ mm}^2$ (0.8% of blockage ratio) and a length of 322 mm. They were scaled to 3.4:1 in comparison with Ahmed's original test

model taking into account the installation of the synthetic jet array. The width of the synthetic jet array, which consists of twelve synthetic jet actuators, matches the length of roof end edge at 120 *mm*. The models were located to a height of 60 *mm* from the wind tunnel floor. The height was determined from preliminary boundary layer thickness measurement.

For the purpose of this study, the synthetic jet array was activated from the roof end edge and the slanted side edges. These two jet locations were chosen because the spanwise vortex from the roof end edge and the horse-shoe streamwise vortices from slanted side edge significantly affect the wake flow region. Although earlier investigations used jets from the roof end edge only [32-34], it is worthwhile to test the effect of jets from the slanted side edges considering the results of Beaudoin and Aider [57]. According to that study, slanted side edges are the best location of flap for lift and drag reduction. Therefore, the wind tunnel models produced here had two parts to change the rear slant angle and the jet location, front and rear sections. Fig. 4.2 shows two configurations of rear section according to the jet location for the 35° slanted model. When the jets emanate from the roof end edge (Fig. 4.2a), the orifices of the synthetic jet array are placed on the roof surface without a space between the roof end edge and the orifice. When the jets emanate from the slanted side edge (Fig. 4.2b), the orifices are placed on slanted surface with a 2 *mm* gap between the orifices and the slanted side edge owing to mechanical limits.

4.1.2 Perpendicular Type Synthetic Jet Actuator

To form a synthetic jet array that satisfied the optimized ratio of the spanwise spacing to the orifice diameter as a means of separation control, a perpendicular type synthetic jet actuator was designed of which the orifice is perpendicular to the oscillating diaphragm [58-59]. The synthetic jet actuator was constructed with three ABS resin plates, a urethane band and a piezoelectric actuator. Fig. 4.3 shows the components of a synthetic jet actuator. Three ABS resin plates form the orifice and the immovable walls of the cavity. The base plate of the piezoelectric actuator is stainless steel, 56 mm in diameter. And the PZT element is a soft PZT type 5A, 50 mm in diameter. The urethane band serves to maintain the seal and to maximize the displacement of the piezoelectric actuator by providing cushioning. The exterior size of one actuator module is 10×60×60 ($w \times h \times l$, mm). The orifice of the synthetic jet actuator is rectangular, with a width of 2 mm along the span and an effective length of 2 mm in the streamwise direction. Figure 4.4 shows the final assembly of the synthetic jet actuator.

The direction of the jet can be changed by replacing the orifice/cavity plate. The jet direction (θ_{jet}) is defined as the angle between the jet and the upper surface in the presence of an exterior flow. Jet directions of $\theta_{jet} = 30^\circ$, 60° and 90° can be demonstrated when the jet emanates from the roof end edge, and $\theta_{jet} = 30^\circ$ and 60° for slanted side edges operation.

To quantify the strength of the synthetic jet, velocity measurements were performed in quiescent air using a hot wire anemometer. A sinusoidal waveform was used to drive a piezoelectric actuator, which is known to

provide the best waveform for a synthetic jet actuator [46]. Fig. 4.5 shows the jet velocity measurement data. With 60 measurement tests according to the amplitude and frequency of the jet driving signal, the relationship between the jet velocity and driving signals was revealed. And then, the jet condition (momentum and frequency) during wind tunnel experiments was determined by interpolating the quiescent jet velocity measurement data.

The strength of a synthetic jet is expressed by the jet momentum coefficient (C_μ), which is defined as

$$C_\mu = n\bar{I}_j / \frac{1}{2} \rho_0 U_0^2 A_0 \quad (4.1)$$

, where n is the number of synthetic jet actuators, \bar{I}_j is the time-averaged momentum during the blowing stroke, ρ_a is the free-stream density, U_0 is the free-stream velocity, and A_0 is frontal area of the wind tunnel model. The time-averaged momentum (\bar{I}_j) is defined as

$$\bar{I}_j = \frac{1}{\tau} \rho_j A_j \int_0^\tau u_j^2(t) dt \quad (4.2)$$

, where τ is the half period of the actuator, ρ_j is the density of the synthetic jet, A_j is the area of the synthetic jet orifice, and $u_j(t)$ is velocity of the synthetic jet. The jet momentum coefficient ranged from $C_\mu = 2.81 \times 10^{-4}$ to 1.80×10^{-2} .

And non-dimensional jet driving frequency is same form with strouhal number, which is defined as:

$$F^+ = \frac{fh}{U_0} \quad (4.3)$$

, where f is the frequency of the jet actuator and h is the height of the wind tunnel model. The range of the jet driving frequency tested was from $F^+ = 0.14$ to 1.74.

4.1.3 Measurement System

In this study, the total aerodynamic drag was instrumented by a single-point high-definition one-axis load cell, the OBU 1004K from Bongsin Co. From specification of manufacturing company, the aerodynamic drag for this wind tunnel model may be measured within an accuracy level of 0.2%. The load cell was located at the center of the bottom surface. The rear surface pressure was instrumented at 32 ports with 16 channel pressure scanners (Net Scanner 9116 by Measurement Specialties) and 16 pressure transducers (SP007 by Delta Metrics). Fig. 4.6 shows the location of the rear pressure ports on the 25° and 35° slanted models. Each surface has 16 ports in a 4×4 grid. Assuming a symmetric flow, all pressure ports are distributed on the left half of the body.

Fig. 4.7 shows schematic of wind tunnel test measurement system. The driving signal for synthetic jet actuator was generated by the DAQ board (NI PCI-6281), connected to HVPZT amplifier (E-481). As the synthetic jet flow

generates, the aerodynamic drag and rear surface pressure was measured. Fig. 4.8 is a picture that the experimental model is installed in the wind tunnel.

The wake flow of Ahmed reference model is fully unsteady. Therefore, the aerodynamic drag and rear surface pressure data contains high degrees of experimental uncertainty. To minimize the uncertainty, the aerodynamic properties without synthetic jet actuation were measured just before the synthetic jet actuation for all experiments. And the properties with synthetic jet actuation were compared with the values that are measured immediately before.

4.1.4 Experimental Parameters

In Table 4.1, all of the experimental parameters and ranges are presented. 620 experimental cases were examined overall for five parameters related to the body configuration and the synthetic jet array actuation. Range of jet driving frequency was determined by jet momentum coefficient. It is because that low driving frequency requiring high jet momentum coefficient and high driving frequency requiring low jet momentum coefficient are not able to be implemented for mechanical limits.

4.2 Flow without Synthetic Jet Actuation

In this section, the aerodynamic drag coefficient (C_D) and rear surface pressure (C_P) distributions without synthetic jet actuation are described. The aerodynamic drag of Ahmed reference model depends on its rear slant angle [31], also the rear wake flow pattern does. In this study, 25° and 35° of slant angle model were chosen for a test model owing different flow topologies. Fig 4.9 shows different flow patterns of 25° and 35° of slant angle model [37]. Wake flow of 25° slant angle model is influenced by spanwise separation from roof end edge and streamwise vortices from slant side edges. On the other hand, streamwise vortices do not exist in the wake of 35° slant angle model. By this difference in wake flow mechanism, the aerodynamic drag of 25° slanted model is larger than that of 35° slanted model.

From this experiment, measured total aerodynamic drag coefficients are $C_D= 0.30$ and 0.26 for slant angles of $\theta_s= 25^\circ$ and 35° , respectively. They are calculated based on the frontal area of the wind tunnel model. Numerically, they are about 4.9% and 2.8% greater than the results of Ahmed *et al.* [31]. The major reason for this slight discrepancy is the difference in the Reynolds number (Re_l). In the present experiments, wind tunnel tests are performed at $Re_l= 4.29 \times 10^5$, which is about 10 times smaller than that of Ahmed *et al.* [31]. In this Reynolds number region, the aerodynamic drag may be increased by reducing the Reynolds number [60].

Fig. 4.10 presents the rear surface pressure distributions without synthetic jet actuation. The horizontal lines at $y/y_h= 0.7$ in Fig. 4.10a and at $y/y_h= 0.55$ in Fig. 4.10b denote the junction between the slanted surface and the vertical

base. The pressure coefficients are classified according to the spanwise location: $z=0$ (center), $0.14w$, $0.28w$ and $0.43w$. From Fig. 4.10, difference in the pressure distribution according to the slant angle is important to note. For $\theta_s=25^\circ$ (Fig. 4.10a), the flow at rear slanted surface is mostly attached. At the pressure ports near the roof end edge ($y/y_h=0.91$), the pressure coefficients are very low. And then, the pressure gradually recovers over the entire rear slanted surface ($0.91 \geq y/y_h \geq 0.74$). There exist streamwise vortices emanating along the slanted side edges. Two pressure ports at $y/y_h=0.74$ and 0.80 when $z=0.43w$ showing relatively low pressures are footprints of the streamwise vortices. The streamwise vortices create a low-pressure region and contribute to the pressure drag. On the other hand, for $\theta_s=35^\circ$ (Fig. 4.10b), detached flow is formed at slanted surface ($0.84 \geq y/y_h \geq 0.61$) and pressure is relatively higher than that of $\theta_s=25^\circ$. Also, there is no pressure recovery on the slanted surface, and the pressure distribution is two-dimensional. For a vertical base, a recirculation region forms, therefore, the pressure at the center is higher than that at the side. The measured rear surface pressure distributions are similar to existing experimental data, and these analyses coincide with the results in earlier work [31,36-38].

4.3 Flow with Synthetic Jet Actuation

4.3.1 Aerodynamic Drag Measurement

This section presents the change in the aerodynamic drag coefficient (ΔC_D) by synthetic jet actuation. Here, the effect of the synthetic jet is discussed according to the jet location, jet direction (θ_{jet}), jet momentum coefficient (C_μ) and jet driving frequency (F^+) on two kinds of slant angles (θ_s). For each jet condition, the measured aerodynamic drag is non-dimensionalized using the drag coefficient of baseline ($C_{D,base}$) for comparison purposes.

In Fig. 4.11, the aerodynamic drag coefficients when the jets emanate from the roof end edge are described. Figs. 4.11a and 4.11b depict the change in the aerodynamic drag coefficient according to the jet momentum coefficient (C_μ) at $F^+ = 0.93$ and jet driving frequency (F^+) at $C_\mu = 2.8 \times 10^{-3}$, respectively. It is expected that the effect of synthetic jet actuation at this location would be similar to that of a roof spoiler. The objective of those jets is to control the spanwise separation from the roof end edge and then to increase the rear surface pressure. In this case, the aerodynamic drag is decreased when $\theta_s = 25^\circ$ but is increased when $\theta_s = 35^\circ$ by the synthetic jet actuation from the roof end edge. When $\theta_s = 25^\circ$, the aerodynamic drag slowly diminishes as the jet momentum coefficient increases, reaching a maximum drag reduction of 5.2%. For the same jet momentum coefficient, the aerodynamic drag is reduced more with a smaller jet angle relative to the oncoming free stream. When $\theta_s = 35^\circ$, there are critical jet momentum

coefficients around $C_{\mu} \approx 1.0 \times 10^{-3}$ which are dependent on the jet direction such that $C_{\mu} \approx 5.02 \times 10^{-4}$ for $\theta_{jet} = 90^\circ$ and $C_{\mu} \approx 1.52 \times 10^{-3}$ for $\theta_{jet} = 30^\circ$ and 60° . When exceeding the critical jet momentum coefficient, the aerodynamic drag is drastically increased. In Fig. 4.11b, jet driving frequency exhibits different dependency from that of the jet momentum coefficient (Fig. 4.11a). When $\theta_s = 25^\circ$, the jet driving frequency does not affect the aerodynamic drag over the tested range from $F^+ = 0.4$ to 1.74 , which is far from the optimum forcing frequency ($F^+ = 0.15$) reported in Brunn and Nitsche [8]. When $\theta_s = 35^\circ$, jet driving frequency shows different dependency with jet direction (θ_{jet}). When $\theta_{jet} = 30^\circ$ and 60° , the jet driving frequency does not affect the aerodynamic drag notably, but when $\theta_{jet} = 90^\circ$, the aerodynamic drag decreases as the jet driving frequency increases. For this case, pressure at the side shows similar distribution regardless of the jet driving frequency, but pressure at the central part is increased as the jet driving frequency increases.

Fig. 4.12 presents the change in the aerodynamic drag coefficient when a pair of synthetic jet arrays is operated from the rear slanted side edges. The objective of these jets is to weaken the streamwise vortices. The streamwise vortices are induced by a low-pressure region on the rear surface, and the aerodynamic drag can be reduced by weakening the streamwise vortices. In this case, however, the synthetic jets on the slanted side edges could not contribute to the reduction of the aerodynamic drag. When $\theta_s = 25^\circ$, there is no direct effect of synthetic jet actuation on the aerodynamic drag (within 0.5%). It appears that once the streamwise vortices are formed, the synthetic jet array configured in present experiment cannot modify the vortices structure. When $\theta_s = 35^\circ$, the aerodynamic drag is increased a little (within 3%). The larger the

jet angle, the more the aerodynamic drag is increased. The jet driving frequency does not have a direct effect on the increase in the aerodynamic drag coefficient (Fig. 4.12b). These results are quite different from Beaudoin and Aider [57]. As mentioned before, slanted side edges were the best location of flap for controlling rear wake. Reason for this different result is brought due to the inherent difference in flow control mechanism between flap and synthetic jet. Flap can reliably change the streamline regardless of the flow conditions. But, synthetic jet may have no effect under the flow condition that the momentum of free stream is much stronger than that of synthetic jet. In this case, the jets from side edges of slanted surface could not affect the flow pattern as well as the aerodynamic drag due to the generation of strong streamwise vortices.

These results show that the aerodynamic drag exhibits different dependency depending on the jet location and the slant angle of the body. In Table 4.2, the average changes in the aerodynamic drag are arranged according to the slant angle and jet location. The aerodynamic drag is decreased only when $\theta_s = 25^\circ$ by jets from the roof end edge. For this case, the jet momentum coefficient has the greatest effect on reducing the aerodynamic drag. However, in other cases, the aerodynamic drag is increased or unchanged by the actuation of the synthetic jet. These changes in the aerodynamic drag are closely related to the alteration of the flow patterns around the rear body. An analysis on the flow pattern will be performed in a later section with flow visualizations and rear surface pressure distribution.

4.3.2 Flow Visualization: Tuft Method

To reveal the change in the rear wake flow caused by the actuation of the synthetic jet, the rear wake flows are visualized using tufts. These steps are performed on the $\theta_s = 25^\circ$ and 35° slanted bodies and the results are compared with the flows without synthetic jet actuation. The jets emanate from the roof end edge to a jet direction of $\theta_{jet} = 60^\circ$. The other operating conditions are a jet momentum coefficient of $C_{\mu} = 6.30 \times 10^{-3}$ and a jet driving frequency of $F^+ = 0.93$. For the purpose of this study, three tufts are suspended above the roof end edge on the symmetry plane ($z = 0$) by a thin nylon wire. The first tuft is located at a height of 5 mm from the roof end edge, and two tufts are positioned at intervals of 10 mm.

Fig. 4.13 presents the flow visualization when $\theta_s = 25^\circ$. In this case, the aerodynamic drag is reduced by 3.4%. When the synthetic jet array is not operated (Fig. 4.13a), the tufts bend to the wind tunnel model, and the tuft on the bottom experiences vibration. And then, as the synthetic jets emanate, the tufts bend to the model slightly more, and the vibration of the first tuft is considerably mitigated; therefore, the first tuft is straightened and more clearly imprinted in Fig. 4.13b. From this, we can see that the momentum transfer by the synthetic jet resulted in stabilization in vicinity of the slanted surface, and the aerodynamic drag reduction.

Fig. 4.14 presents the flow visualization when $\theta_s = 35^\circ$. For this case, the aerodynamic drag is increased by 24.5%. When the synthetic jet array is not operated (Fig. 4.14a), all tufts point toward the free-stream direction because separation has occurred at the roof end edge. And then, as the synthetic jet

array operates (Fig. 4.14b), all tufts bend toward the wind tunnel model, and severe vibration on the first tuft is observed. Therefore the first tuft is scarcely visible in Fig. 10b. Thus, due to the synthetic jets, the separation from the roof end edge is suppressed but the flow around the rear body becomes unstable.

Changes of the center flow according to the synthetic jet actuation are shown when $\theta_s = 25^\circ$ (Fig. 4.13) and 35° (Fig. 4.14). In both cases, the spanwise vortex is suppressed but the aerodynamic drag is decreased for $\theta_s = 25^\circ$ and increased for $\theta_s = 35^\circ$. This reveals that the suppression of the spanwise separation is not directly linked to the reduction in the aerodynamic drag. For some steep configurations, the aerodynamic drag can be increased by suppressing the separation.

4.3.3 Rear Surface Pressure Measurement

The rear surface pressure distribution offers a plausible explanation of the change in the aerodynamic drag. To go further in this analysis, rear surface pressure distributions are analyzed to compare the wake flow with and without actuation of the synthetic jet.

Figs. 4.15-16 show the rear surface pressure distributions when $\theta_s = 25^\circ$ and 35° , respectively. The closed symbol denotes the flow without synthetic jet actuation, and the open symbol denotes the flow with synthetic jet actuation. In both cases, the jets emanated from roof end edge, and the other operating conditions of the synthetic jet array are as follows: $\theta_{jet} = 60^\circ$ and $C_{\mu} = 2.83 \times 10^{-3}$, 1.09×10^{-2} with the corresponding jet driving frequencies. Each

datum is the averaged pressure coefficient over the jet driving frequencies.

When $\theta_s = 25^\circ$ (Fig. 4.15), the aerodynamic drag is reduced by 2.05% and 4.29% when $C_\mu = 2.83 \times 10^{-3}$ and 1.09×10^{-2} , respectively. As the synthetic jet array is operated, the increase in the pressure at the slanted surface is noticeable, but there is little change at the vertical base. To explain the reason why the pressure is changed only at the rear slant surface, we need to observe the flow without synthetic jet actuation attentively. For the flow without synthetic jet actuation, the attached flow is formed at rear slanted surface, and then, the flow is separated from the junction between the slanted surface and the vertical base.

In case that synthetic jet is activated, the aerodynamic drag is decreased as C_μ is increased (Fig. 4.11a). As shown in Fig. 4.16, pressure distributions at the vertical base are almost the same with increase of C_μ . It means that the transferred momentum by the synthetic jet actuation does not affect pressure distribution at the vertical base and the flow structure does not change. It only contributes to increase pressure in the vicinity of the slanted surface. Accordingly, the streamwise vortices are weakened with the synthetic jet actuation (Fig. 11d), then, the aerodynamic drag decrease. In addition, the larger C_μ leads to the less aerodynamic drag.

When $\theta_s = 35^\circ$ (Fig. 4.16), the aerodynamic drag increases by 20.5% and 18.4% when $C_\mu = 2.83 \times 10^{-3}$ and 1.09×10^{-2} , respectively. Here, unlike the case above ($\theta_s = 25^\circ$), the notable pressure change occurred both at the slanted surface and at the vertical base surface. For the flow without synthetic jet actuation, the separation occur at the roof end edge (Fig. 4.14a), therefore, the pressure at the slanted surface is much higher than that of $\theta_s = 25^\circ$ (Fig. 4.10).

In case that the synthetic jet is activated, the aerodynamic drag is significantly increased as depicted in Fig 4.11a. As shown in Fig. 4.16, the pressure at the slanted surface is significantly decreased, and the pressure recovery through the entire slanted surface is observed. This pressure distribution upon the actuation of the synthetic jet is quite similar to the flow for $\theta_s = 25^\circ$. The reason why this flow pattern appears is that the flow is attached to the slanted surface by the transferred momentum of the synthetic jet. The flow is accelerated as passing the slanted surface and leads to the low pressure region in the vicinity of the slanted surface. Accordingly, the side flow is rushing into the slanted surface so that it makes strong streamwise vortices which increase the aerodynamic drag.

In present experiments, a fairly large rise in the aerodynamic drag is appeared. Considering the result of Groche and Meier [61], this result is reasonable. From their research, they eliminated the streamwise vortices by applying slender conical shape for the rear part, and achieved drag reduction by more than 50% for the wind tunnel model.

4.3.4 Tests for the Number and Position of the Activated Jet in the Actuator Array

From the former experimental set, the effects of various operating parameters are revealed. This section presents additional experiments performed to assess the effect of number and position of the activated jets in the actuator array. Tests are performed on the $\theta_s = 25^\circ$ slanted body, and the

jets emanate from the roof end edge at a jet direction of $\theta_{jet} = 60^\circ$. The configured jet array consists of twelve synthetic jet actuators. In the former experiments, all of the jet actuators are activated, but here the numbers and positions of the activated jets are changed to find the effective distribution for the reduction of the aerodynamic drag. Eight and four activated jet actuators are tested. In each case, the positions of the jets are changed from the center to the side of the roof end edge. Five cases in total are tested according to the distribution of the activated jets. For each case, 34 experiments are performed according to the jet momentum coefficient with the corresponding jet driving frequency. The jet momentum coefficients range from $C_{\mu} = 4.4 \times 10^{-3}$ to 1.09×10^{-2} . The measured aerodynamic drag coefficients are averaged for each case and compared with all actuators operated cases. The efficiency of each jet is defined while considering the amount of electric power consumed, and compared to all others.

The experimental conditions and results are summarized in Table 4.3 and also depicted in Fig. 4.17. From a simple comparison of the total aerodynamic drag reduction amounts, the greatest drag reduction is achieved when all of the actuators are activated. With eight activated jets, drag reductions ranging from 44.8% to 86.7% are achieved, and the range is from 18.8% to 53.9% for four activated jets. From this, it is clear that wherever a synthetic jet actuator is activated along with the roof end edge, the jets contribute to the drag reduction. And packed jet actuators in the center of roof end edge have an advantage to maximize the aerodynamic drag reduction. In addition, the efficiency of the jets provides an interesting point of view. The efficiency is defined by the reduction of aerodynamic drag coefficient divided by the jet

momentum coefficient of activated jets. Because the electric power used to operate a synthetic jet actuator is proportional to the generated jet momentum, this metric can be considered as a measure of the efficiency of the jet. The fifth column shows that even the total amount of drag reduction diminishes with fewer activated jets, whereas the efficiency increases when the jets are concentrated on the central part of the roof end edge. In Fig. 4.17, the efficiency of jet is depicted. It shows that the aerodynamic drag reduction may not be as much as jet input momentum, when the jets emanate from the side of roof end edge (case 3 and 6). The most effective jet distribution is shown when four jet actuators are operated at the central part (case 4). Therefore, it is clear that to reduce aerodynamic drag by controlling the spanwise separation, the effective actuator location is the central part of the rear edge. This represents there can exist the optimal number of synthetic jet actuators to maximize the drag reduction while minimizing the electric power consumption.

Table 4.1 Range of experimental parameters

Parameter	Range	
Slant angle, θ_s (2 configurations)	25°, 35°	
Jet location (2 cases)	Roof end edge	Slanted side edges
Jet direction, θ_{jet} (2 or 3 cases)	30°, 60°, 90°	30°, 60°
Jet momentum coefficient, C_μ (8 cases)	2.34×10 ⁻⁴ , 5.02×10 ⁻⁴ , 1.52×10 ⁻³ , 2.83×10 ⁻³ , 4.43×10 ⁻³ , 6.31×10 ⁻³ , 8.48×10 ⁻³ , 1.09×10 ⁻²	
Jet driving frequency, F^+ (11 cases)	0.40, 0.53, 0.67, 0.80, 0.93, 1.07, 1.20, 1.34, 1.47, 1.60, 1.74 (F^+ is determined by C_μ)	
Total	620 cases	

Table 4.2 Change in aerodynamic drag according to slant angle and actuator location

Slant angle	Jet location	$\Delta C_D / C_{D,Base}^{1)}$ [%]
25°	Roof end edge	-2.91
	Slanted side edges	-
35°	Roof end edge	+20.54
	Slanted side edges	+2.74

¹⁾: Averaged by jet direction, jet momentum coefficient and jet driving frequency conditions.

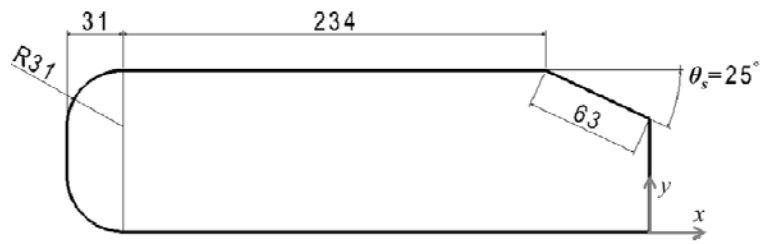
Table 4.3 Aerodynamic drag reduction according to the number and positions of activated jet actuators

Case No.	Number of activated jets (corresponding C_μ)	Activated jet position in the actuator array ¹⁾	$\Delta C_D/C_{D,Base}$ ²⁾ [%] (Relative ratio)	Efficiency of jet, $-\Delta C_D/C_\mu$ (Relative Ratio)
1	12 ($C_\mu = 7.53 \times 10^{-3}$)	111111111111	-3.75 (100.0)	1.47 (100)
2	8 ($C_\mu = 5.02 \times 10^{-3}$)	001111111100	-3.25 (86.7)	1.92 (130)
3		111100001111	-1.68 (44.8)	0.99 (67)
4	4 ($C_\mu = 2.51 \times 10^{-3}$)	000011110000	-2.02 (53.9)	2.38 (161)
5		001100001100	-1.77 (47.2)	2.09 (142)
6		110000000011	-0.70 (18.8)	0.82 (56)

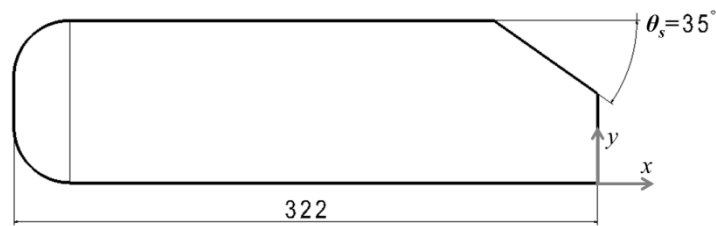
¹⁾: '1' and '0' denote jet on and off location, respectively.

²⁾: Averaged by jet momentum coefficient and jet driving frequency conditions.

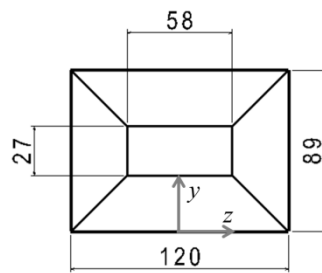
* : Jet distribution showing higher efficiency than all jet actuators activation



(a) Side view, $\theta_s = 25^\circ$

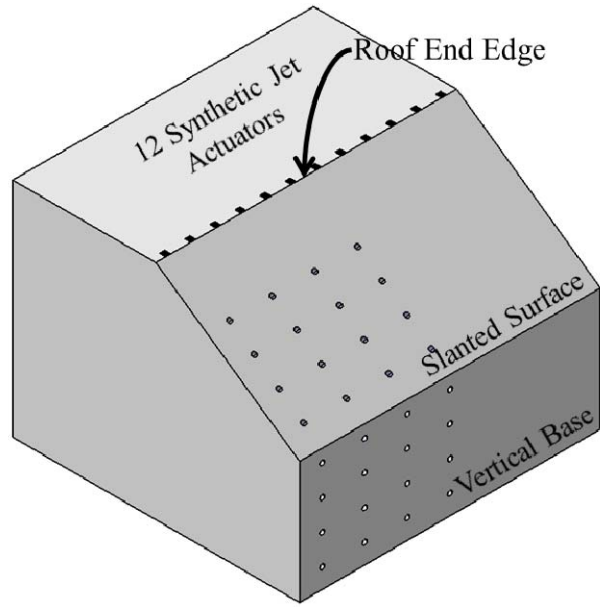


(b) Side view, $\theta_s = 35^\circ$

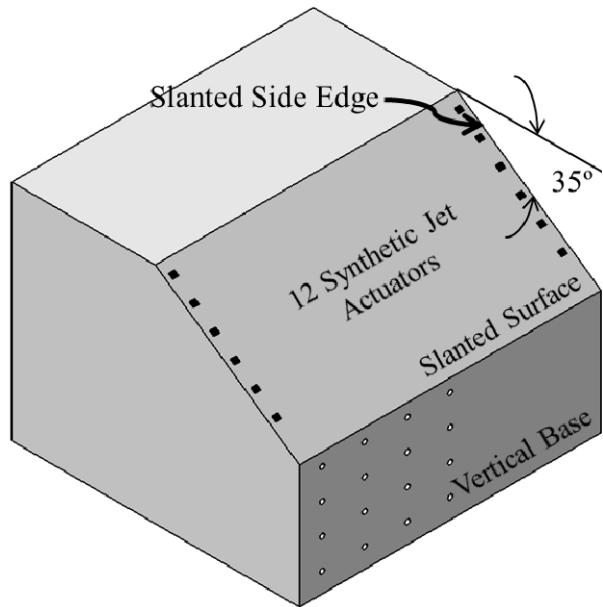


(c) Front-end view

**Fig. 4.1 Geometry of Ahmed body for present experiments
(dimensions given in mm)**



(a) Roof end edge jets.



(b) Slanted side edge jets.

Fig. 4.2 Two rear sections according to the jet location for $\theta_s = 35^\circ$

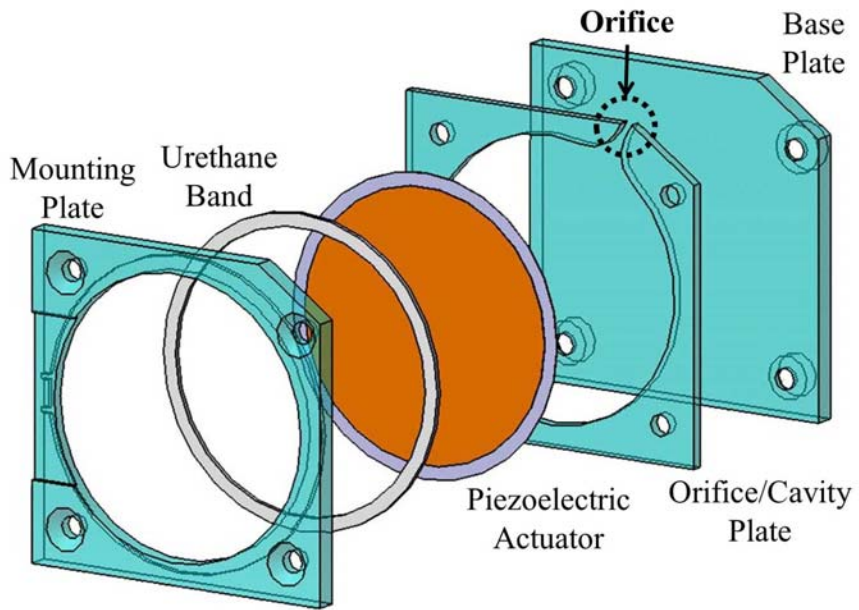


Fig. 4.3 Components of perpendicular type synthetic jet actuator

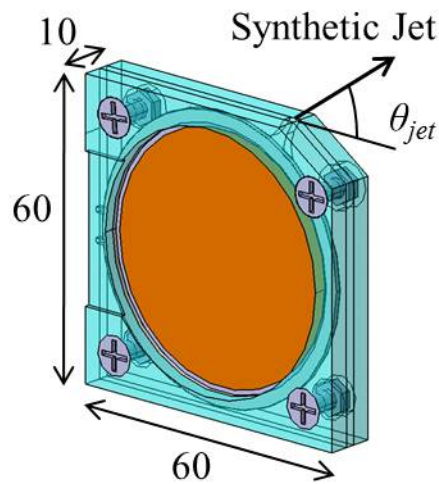


Fig. 4.4 Final assembly of perpendicular type synthetic jet actuator

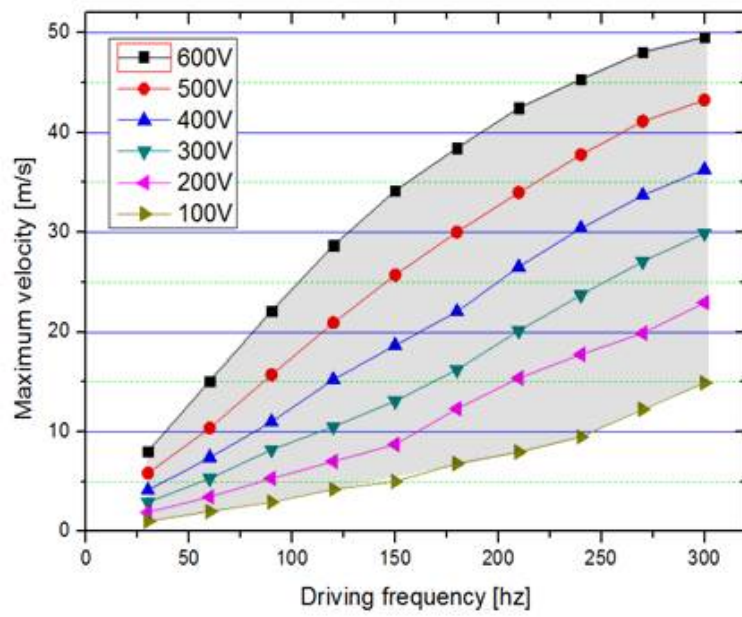
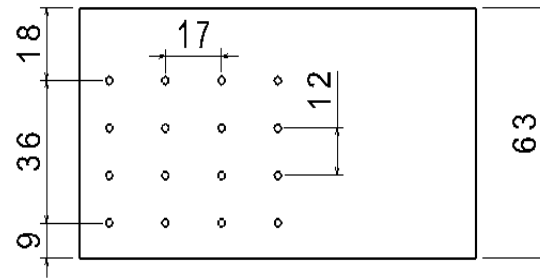
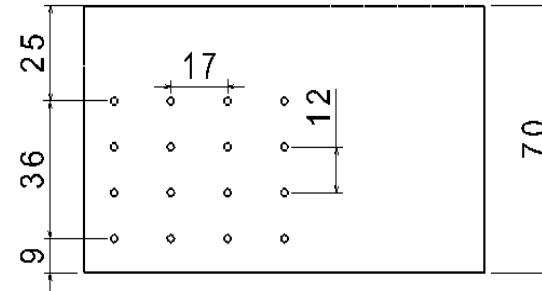


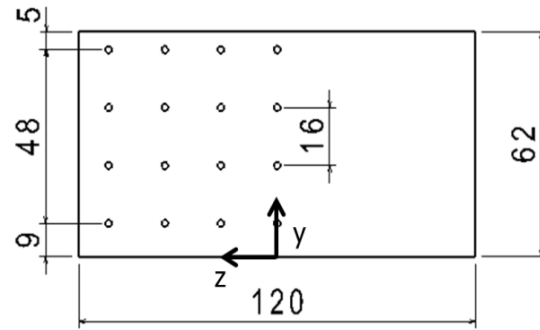
Fig. 4.5 Synthetic jet velocity measurements in quiescent condition



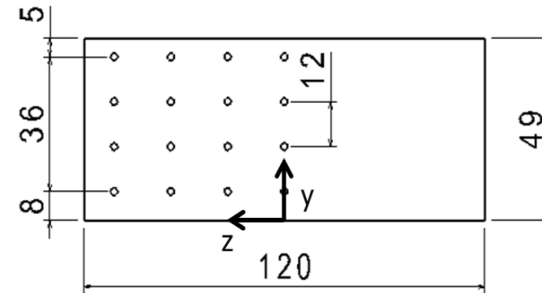
(a) Slanted surface, $\theta_s = 25^\circ$



(b) Slanted surface, $\theta_s = 35^\circ$



(c) Vertical base, $\theta_s = 25^\circ$



(d) Vertical base, $\theta_s = 35^\circ$

Fig. 4.6 Pressure ports on rear surface (dimensions given in *mm*)

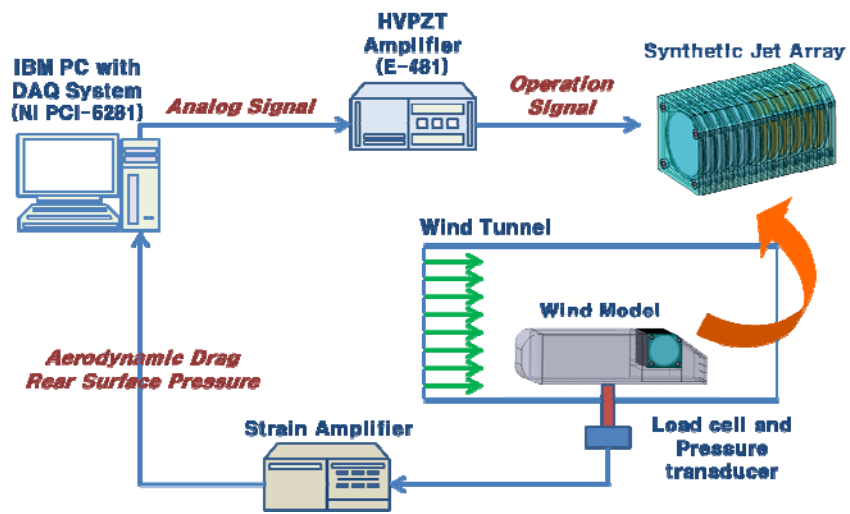
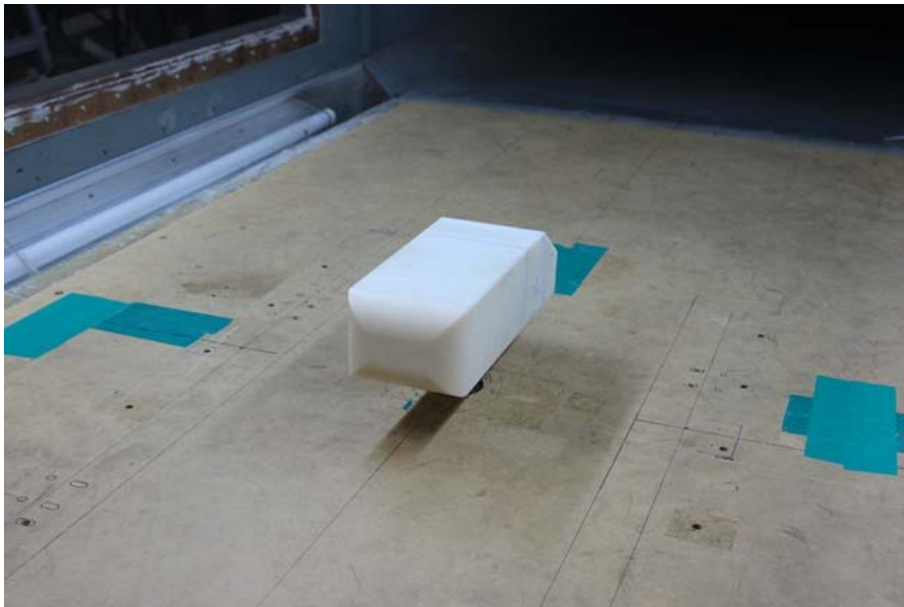


Fig. 4.7 Schematic of wind tunnel test measurement system

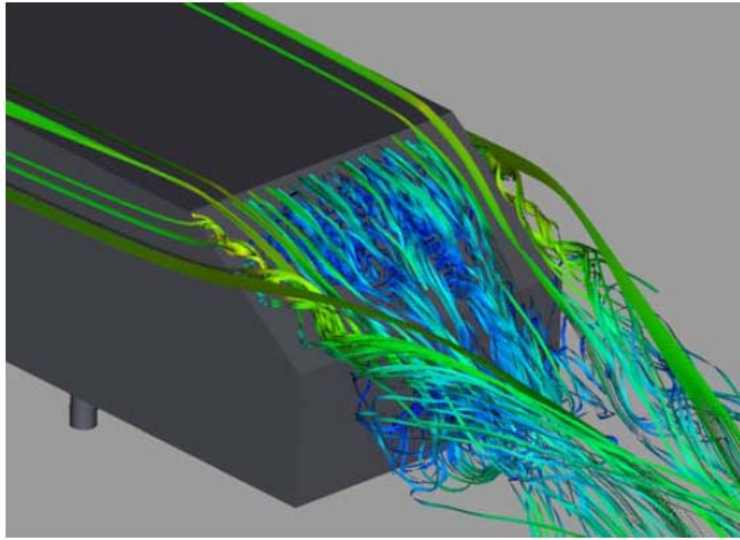


(a) Front-view

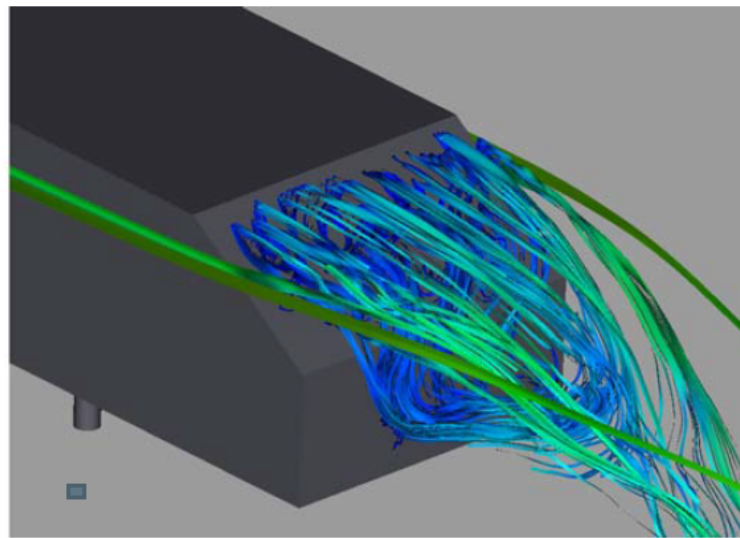


(b) Iso-view

Fig. 4.8 Wind tunnel model in SNU wind tunnel

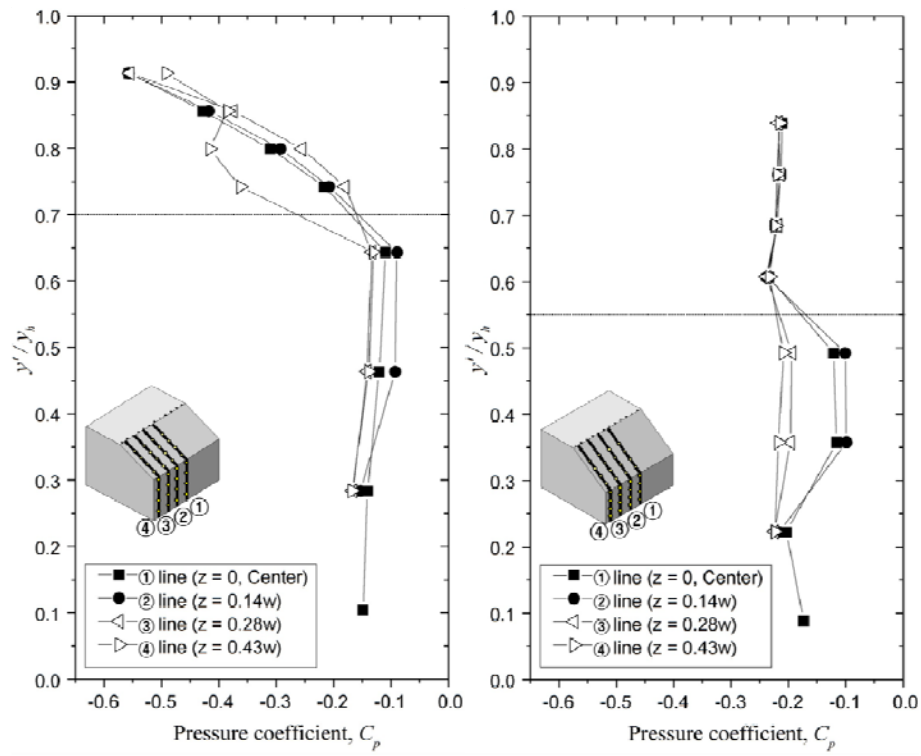


(a) $\theta_s = 25^\circ$



(b) $\theta_s = 35^\circ$

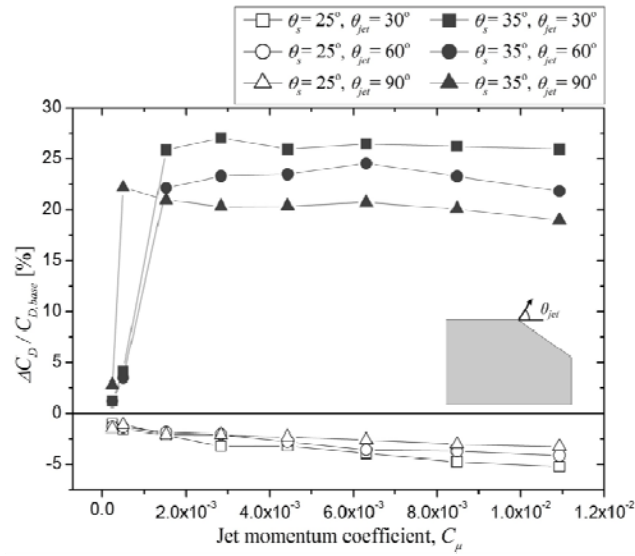
Fig. 4.9 Rear wake flow of Ahmed reference model [37]



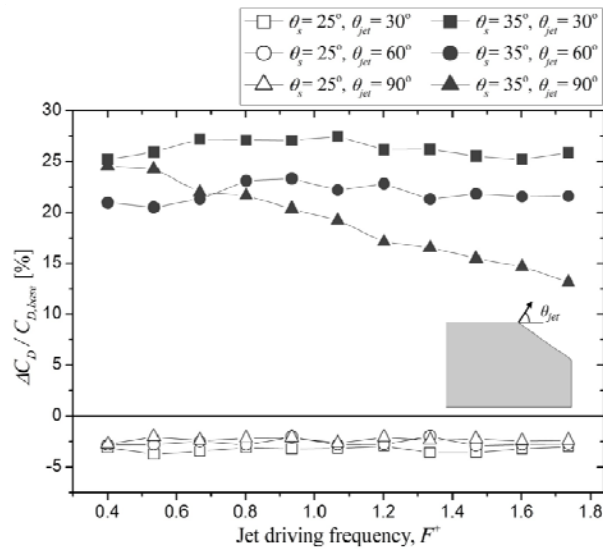
(a) $\theta_s = 25^\circ$

(b) $\theta_s = 35^\circ$

Fig. 4.10 Rear surface pressure distribution of a flow without synthetic jet actuation

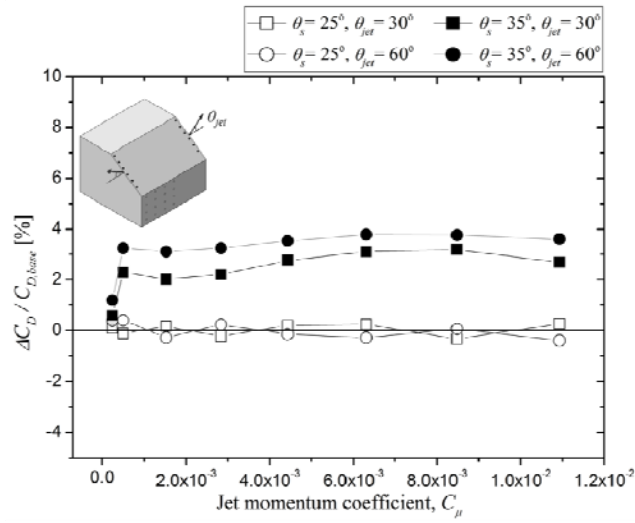


(a) Influence of jet momentum coefficient (C_μ) for $F^+ = 0.93$

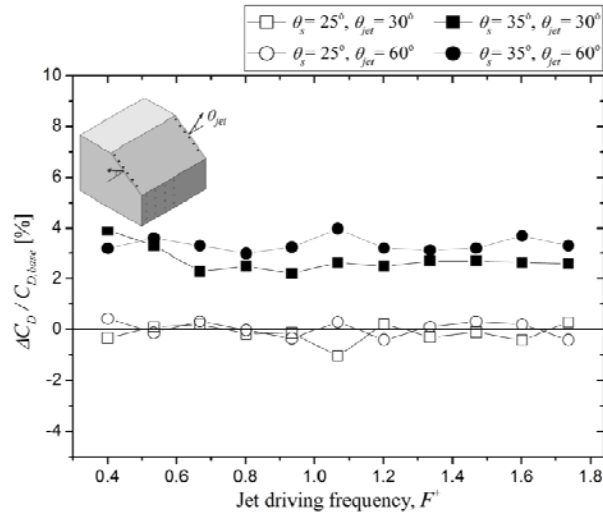


(b) Influence of jet driving frequency (F^+) for $C_\mu = 2.8 \times 10^{-3}$

Fig. 4.11 Change in aerodynamic drag by synthetic jet array actuation from roof end edge

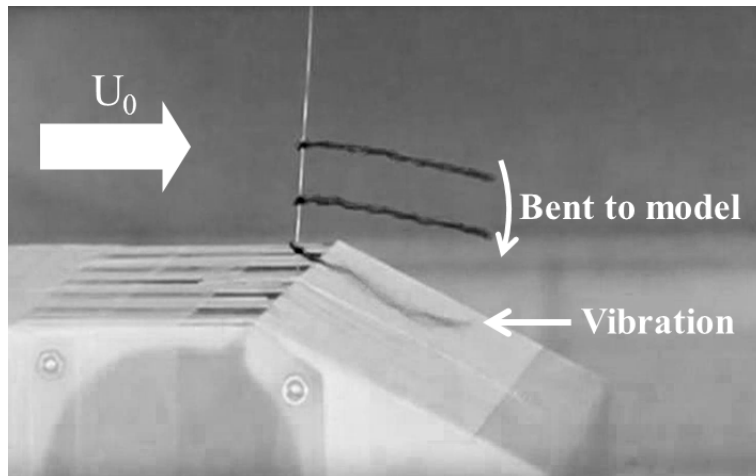


(a) Influence of jet momentum coefficient (C_μ) for $F^+ = 0.93$

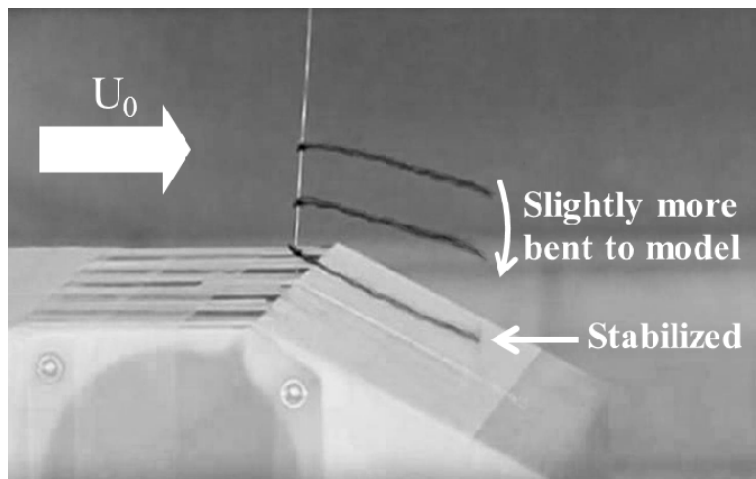


(b) Influence of jet driving frequency (F^+) for $C_\mu = 2.8 \times 10^{-3}$

Fig. 4.12 Change in aerodynamic drag by synthetic jet arrays actuation from slanted side edges

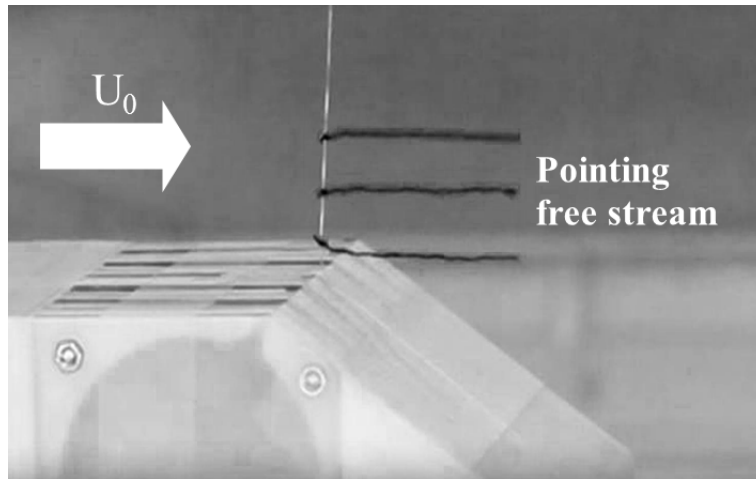


(a) Flow without synthetic jet actuation

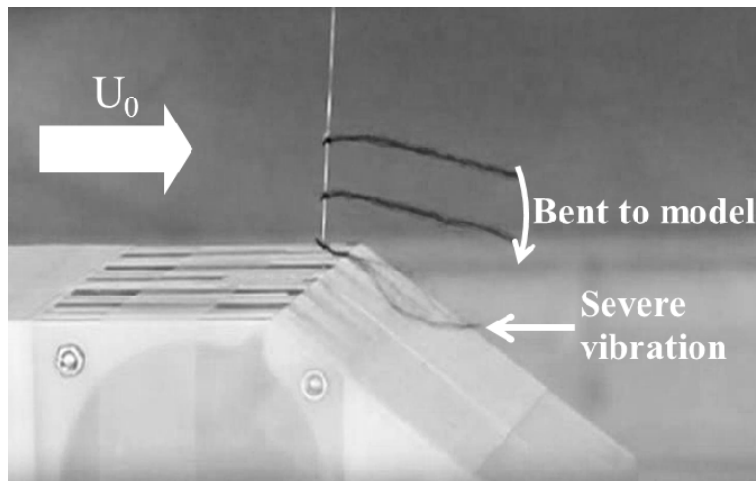


(b) Flow with synthetic jet actuation from roof end edge

Fig. 4.13 Rear wake flow visualization for $\theta_s = 25^\circ$

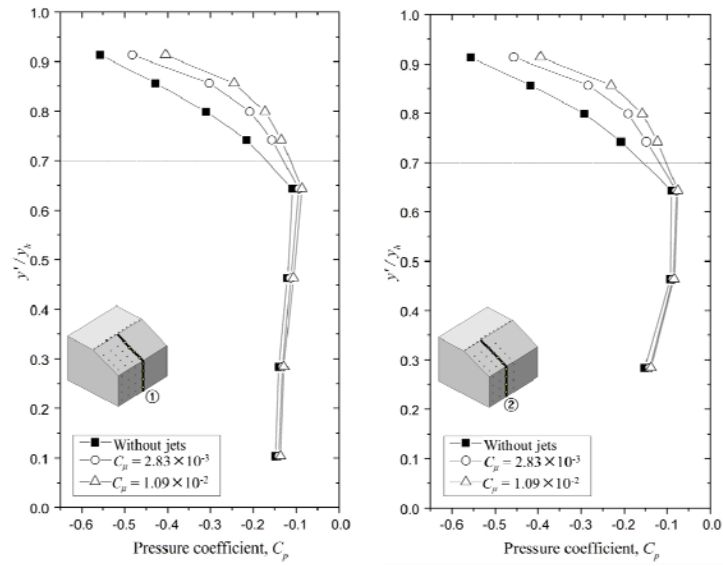


(a) Flow without synthetic jet actuation



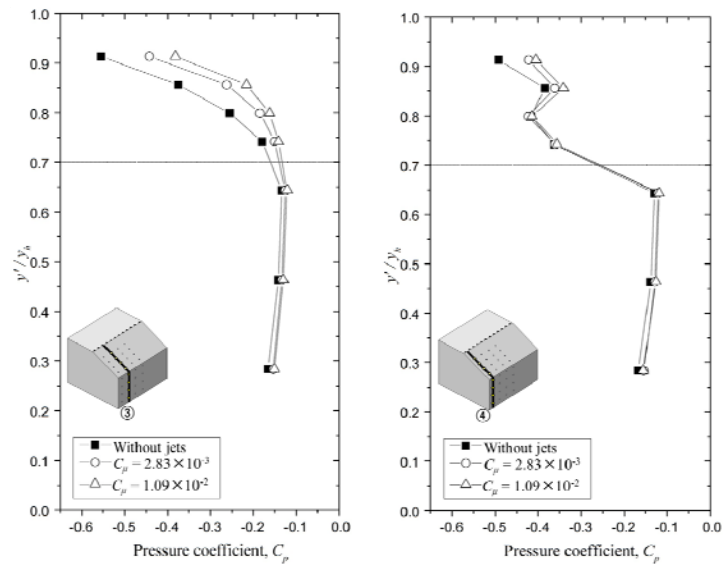
(b) Flow with synthetic jet actuation from roof end edge

Fig. 4.14 Rear wake flow visualization for $\theta_s = 35^\circ$



(a) At $z=0$ (center)

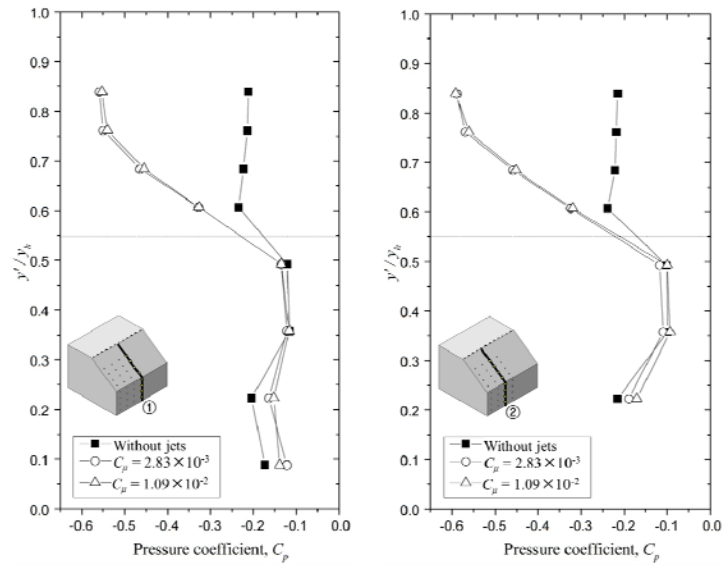
(b) At $z=0.14w$



(c) At $z=0.28w$

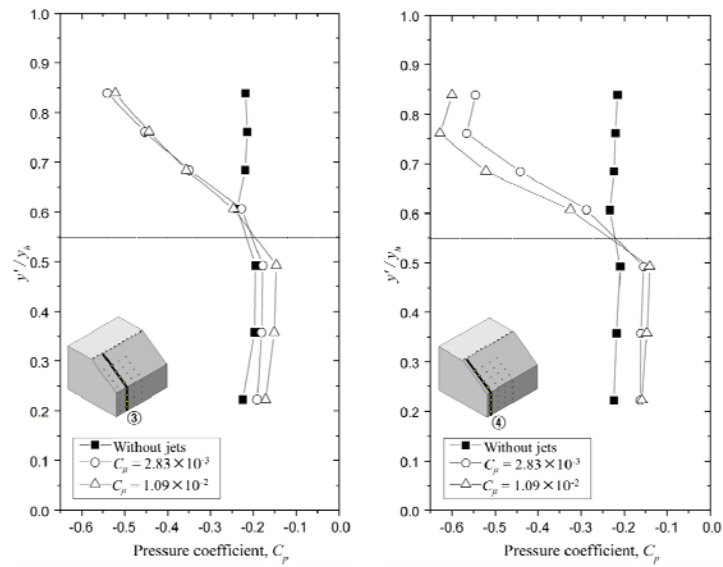
(d) At $z=0.43w$

Fig. 4.15 Rear surface pressure distributions for $\theta_s=25^\circ$ with and without synthetic jets from roof end edge



(a) At $z=0$ (center)

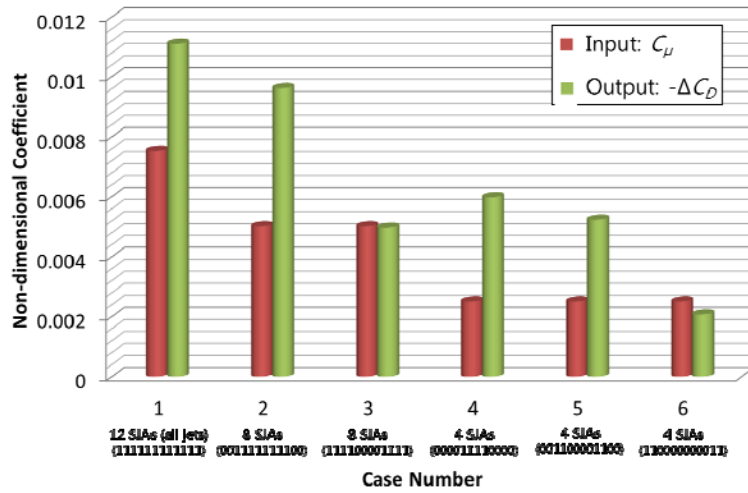
(b) At $z=0.14w$



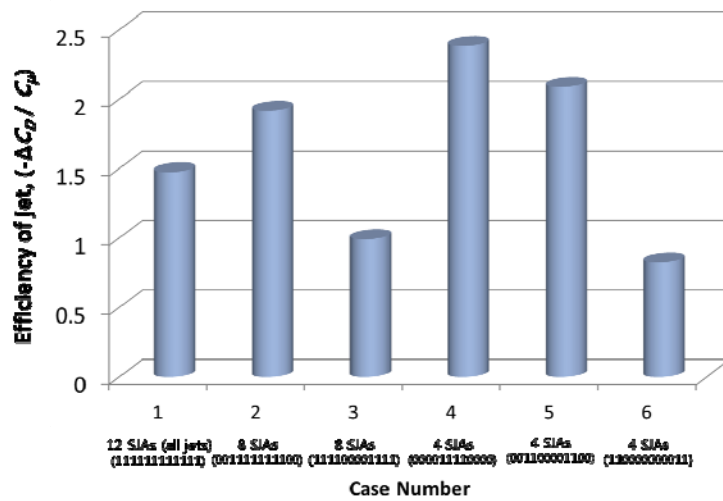
(c) At $z=0.28w$

(d) At $z=0.43w$

Fig. 4.16 Rear surface pressure distributions for $\theta_s=35^\circ$ with and without synthetic jets from roof end edge



(a) Comparison of jet momentum coefficient and drag coefficient reduction



(b) Efficiency of jet

Fig. 4.17 Efficiency of jet according to the number and positions of activated jet actuators

Chapter 5. Conclusions

This study is focused on the synthetic jet as a means of flow control method. At first, parametric study on the geometry of the synthetic jet actuator is conducted and optimal design procedure is followed. The effects of orifice length, cavity depth and jet driving frequency on the synthetic jet velocity are studied for an axisymmetric parallel type of synthetic jet actuator. And then, the effect of the actuation of a synthetic jet array on the aerodynamic drag of a three-dimensional simplified car body (the Ahmed reference model) is intensively investigated. For two configurations of an Ahmed body (slant angles of $\theta_s= 25^\circ$ and 35°), wind tunnel tests were performed under various operating conditions of a synthetic jet array. The parameters considered are the jet location, jet direction, jet momentum coefficient, jet driving frequency, and the number and position of activated jets in the actuator array. From the results, the principal findings are listed below.

- 1) Synthetic jet velocity is significantly affected by the jet driving frequency because of cavity resonance. For most of actuator configurations, a single resonance frequency was observed and the maximum velocity was observed at this frequency which depends on the geometry variables. However, for a small cavity depth (5 mm), the jet velocity was not decreased after the cavity resonance frequency, but rather increased a little. In general, the smaller orifice length and cavity depth, the larger maximum jet velocity. But, optimum length

exists for orifice length.

- 2) The wake flow controllability by the synthetic jet array is dependent on the base shape of the body and the jet location. For the $\theta_s = 25^\circ$ slanted body, the rear flow is controlled to reduce the aerodynamic drag when the jets emanate from the roof end edge. In this case, synthetic jet actuation contributes to suppressing the spanwise vortex, which increases the slanted surface pressure by supplying momentum to the flow field. The maximum drag reduction is 5.2%. However, the aerodynamic drag is unchanged by the jets from the slanted side edges. On the other hand, for the 35° slanted body, the actuation of the synthetic jet leads to an increase in the aerodynamic drag for both jet locations. Particularly, jets emanating from the roof end edge drastically increase the aerodynamic drag with inducing the streamwise vortices.
- 3) The effects of various operating parameters on the aerodynamic drag were revealed. In the experiments, the aerodynamic drag is decreased with the $\theta_s = 25^\circ$ slanted body by jets emanating from the roof end edge. For this jet condition, the reduction of the aerodynamic drag has a tendency to be proportional to the jet momentum coefficient. And, for a smaller jet angle relative to the free stream, the aerodynamic drag is reduced more. However, the jet driving frequency has no direct effect on aerodynamic drag over the tested range.

- 4) Regarding number and positions of the activated jet test, the efficiency of a jet is defined considering the amount of electric power consumed, and comparisons are made with various distributions of jets. The result identified the effective distribution of jets. In comparison with the condition in which all jets are actuated, the aerodynamic drag is effectively reduced when the activated jets are concentrated on the central parts of the roof end edge. There can exist optimized number of synthetic jet actuators to maximize the aerodynamic drag reduction with minimal electric power consumption.

Based on present findings, applying a synthetic jet array to a commercial vehicle to reduce the aerodynamic drag is an appropriate future work in this line of research.

References

- [1] <http://www.knoc.co.kr/>
- [2] <http://www.law.go.kr/>
- [3] J. Howell, C. Sherwin, M. Passmore, and G. Le Good, "Aerodynamic Drag of a Compact SUV as Measured On-road and in the Wind Tunnel." *SAE Technical Paper*, 2002, No. 2002-01-0529.
- [4] W.-H. Hucho, "Aerodynamics of Road Vehicles from Fluid Mechanics to Vehicle Engineering 4th edn.," Cambridge Univ. Press, London, UK 1998.
- [5] S. O. Kang, "Design Optimization and Active Flow Control for Automotive Aerodynamic Drag Reduction", Ph. D. Thesis, Seoul National University, Seoul, Korea, 2012.
- [6] Gad-el-Hak, "Flow Control: Passive, Active, and Reactive Flow Management," Cambridge Univ. Press, New York, USA 2009.
- [7] B. Smith, and A. Glezer, "The formation and Evolution of Synthetic Jets," *Phys. Fluids*, Vol. 10, No. 9, 1998, pp. 2281-2297
- [8] M. Amitay, B. Smith, and A. Glezer, "Aerodynamic Flow Control using Synthetic Jet Technology," *36th AIAA Aerospace Sciences Meeting and Exhibit*, 12-15 January 1998, Reno, NV.
- [9] A. Crook, A. M. Sadri, and N. J. Wood, "The Development and Implementation of Synthetic Jets for the Control of Separated Flow," *17th AIAA Applied Aerodynamics Conference*, June 28 - July 1 1999, Norfolk, VA.

- [10] D. Greenblatt, and I. Wygnanski, "Control of Separation by Periodic Excitation," *Progress in Aerospace Science*, Vol. 37, No. 7, 2000, pp. 487-545
- [11] M. Amitay, D. R. Smith, V. Kibens, D. E. Parekh, and A. Glezer, "Aerodynamic Flow Control over an Unconventional Airfoil using Synthetic Jet Actuators," *AIAA Journal*, Vol. 39, No. 3, 2001, pp. 361-370
- [12] L. W. Traub, A. Miller, and O. Rediniotis, "Effects of Synthetic Jet Actuation on a Ramping NACA 0015 airfoil," *Journal of Aircraft*, Vol. 41, No. 5, 2004, pp. 1153-1162.
- [13] B. L. Smith, and A. Glezer, "Jet Vectoring Using Synthetic Jets," *Journal of Fluid Mechanics*, Vol. 458, 2002, pp. 1-34.
- [14] H. Wang, and S. Menon, "Fuel-Air Mixing Enhancement by Synthetic Microjets," *AIAA Journal*, Vol. 39, No. 12, 2001, pp. 2308-2319.
- [15] A. Pavlova, and M. Amitay, "Electronic Cooling using Synthetic Jet Impingement," *Journal of Heat Transfer*, Vol. 128, No. 9, 2006, pp. 897-907.
- [16] A. Santhanakrishnan and J. D. Jacob, "Flow Control with Plasma Synthetic Jet Actuators," *J. Phys. D: Appl. Phys.*, Vol. 40, 2007, pp. 637-651
- [17] G. A. Slipper, and J. E. Hubbard Jr, "Description and Characterisation of an Electroactive Polymer Synthetic Jet Actuator," *Proc. SPIE – Electroactive Polym. Actuators Devices*, 2007, No. 6524, pp. 1-12.
- [18] S. Lee, K. J. Kim and H. C. Park, "Modeling of an IPMC Actuator-driven Zero-net-mass-flux Pump for Flow Control," *J. Intell. Mater. Systems*

- Struct.*, 2006, No. 17, pp. 533-541.
- [19] Y. Liang, Y. Kuga and M. Taya, "Design of Membrane Actuator Based on Ferromagnetic Shape Memory Alloy Composite for Synthetic Jet Applications," *Sensors Actuators A: Physical*, 2006, No. 125, pp. 512-518.
- [20] P. Mane, K. Mossi and R. Bryant, "Experimental Design and Analysis for Piezoelectric Circular Actuators in Flow Control Applications," *Smart Mater. Struct.*, 2008, No. 17, Vol. 1-12.
- [21] J. M. Shuster and D. R. Smith, "Experimental Study of the Formation and Scaling of a Round Synthetic Jet," *Phys. Fluids*, Vol. 19, 2007, No. 045109, pp. 1-27.
- [22] W. R. Kim, "Experimental Study on Active Flow Control of Synthetic Jets depending on Exit Configuration," Ph. D. Thesis, Seoul National University, Seoul, Korea, 2011.
- [23] M. Jabbal, S. Liddle, J. Potts and W. Crowther, "Development of Design Methodology for Synthetic Jet Actuator Array for Flow Separation Control Applications," *6th AIAA Flow Control Conference*, 25-28 June 2012, New Orleans, Louisiana
- [24] G. Godard and M. Stanislas, "Control of a Decelerating Boundary Layer. Part 1: Optimisation of Passive Vortex Generators," *Aerospace Sci. Technol.*, Vol. 10, 2006, No. 3, pp. 181-191.
- [25] G. Godard and M. Stanislas, "Control of a Decelerating Boundary Layer. Part 3: Optimisation of Round Jets Vortex Generators," *Aerospace Sci. Technol.*, Vol. 10, 2006, No. 6, pp. 455-464.
- [26] W. J. Crowther, "Control of Separation on a Trailing Edge Flap using Air

- Jet Vortex Generators,” *Journal of Aircraft*, Vol. 45, 2006, No. 5, pp. 1589-1593.
- [27] J.E. Cater and J. Soria, “The Evaluation of Round Zero-net-mass-flux Jets,” *J. Fluid Mech.*, Vol. 472, 2002 167.
- [28] Y. Utturkar, R. Holman, R. Mittal, B. Carroll, M. Sheplak, L. Cattafesta, “A Jet Formation Criteria for Synthetic Jet Actuators,” *41st Aerospace Sciences Meeting & Exhibit*, 6-9 January 2003, Reno, NV
- [29] R. Holman, Y. Utturkar, R. Mittal, B.L. Smith and L. Cattafesta, “Formation Criterion for Synthetic Jets,” *AIAA Journal*, 43 (2005) 2110.
- [30] A. Agrawal and G. Verma, “Similarity Analysis of Planar and Axisymmetric Turbulent Synthetic Jets,” *Int. J. Heat and Mass Transfer* Vol. 51, 2008, pp. 6194-6198.
- [31] S. R. Ahmed, G. Ramm and G. Faltin, “Some Salient Features of the Time-Averaged Ground Vehicle Wake,” *SAE Technical Paper*, 1984, No.840300.
- [32] C. Leclerc, E. Levallois, P. Gilliéron, and A. Kourta, “Aerodynamic Drag Reduction by Synthetic Jet: A 2D Numerical Study around a Simplified Car,” *3rd AIAA Flow Control Conference*, 5-8 June 2006, San Francisco, California.
- [33] A. Brunn and W. Nitsche, “Active Control of Turbulent Separated Flows over Slanted Surfaces,” *International Journal of Heat and Fluid Flow*, Vol. 27, 2006, pp. 748–755.
- [34] A. Brunn, E. Wassen, D. Sperber, W. Nitsche and F. Thiele, “Active Drag Control for a Generic Car Model,” *Notes on Numerical Fluid Mechanics and Multidisciplinary Design*, Vol. 95, 2007, pp. 247-259.

- [35] F. Browand , R. McCallen and J. Ross (Eds.), “The Aerodynamics of Heavy Vehicles: Trucks, Buses, and Trains,” Springer Verlag, ISBN: 3-540-22088-7, 2004
- [36] H. Lienhart and S. Becker, “Flow and Turbulence Structure in the Wake of a Simplified Car Model,” *SAE Technical Paper*, 2003, No.2003-01-0656.
- [37] F. Ehab, “Unsteady Flow Simulation of the Ahmed Reference Body using a Lattice Boltzmann Approach,” *Computers & Fluids*, Vol. 35, 2006, pp. 940-950.
- [38] E. Guilmineau, “Computational Study of Flow around a Simplified Car Body,” *Journal of Wind Engineering and Industrial Aerodynamics*, Vol. 96, 2008, pp. 1207-1217.
- [39] F. M. White, “Fluid Mechanics 5th edition,” *McGraw Hill*, 2003.
- [40] <http://www.efunda.com/>
- [41] F. E. Jørgensen, “How to Measure Turbulence with Hot-wire Anemometers - a Practical Guide,” *Dantec Dynamics*, 2002
- [42] <http://www.loadcelltheory.com/>
- [43] <http://www.transducertechniques.com/>
- [44] R. S. Figliola and D. E. Beasley, “Theory and Design for Mechanical Measurements,” John wiley & Sons, Inc., 1995.
- [45] E. O. Doebelin, “Measurement Systems Application and Design 4th Edition,” McGraw Hill, 1990
- [46] K. Mossi, N. D. Castro, R. Bryant and P. Mane, “Boundary Condition Effects on Piezo-Synthetic Jets,” *Integrated Ferroelectrics*, Vol. 71, 2005 No. 1, pp. 257- 266

- [47] Y. L. Vargas, T. J. Finley and K. Mohseni, "Flow Characterization of a Synthetic Jet", *44th AIAA Aerospace Sciences Meeting and Exhibit*, 9 – 12, January, 2006, Reno, Nevada
- [48] M. Chaudhari, B. Puranik and A. Agrawal, "Frequency Response of a Synthetic jet Cavity," *Exp. Thermal Fluid Sci.*, Vol. 33, No. 3, 2009, pp. 439-448.
- [49] M. Jain, B. Puranik and A. Agrawal, "A Numerical Investigation of Effects of Cavity and Orifice Parameters on the Characteristics of a Synthetic Jet Flow," *Sensors and Actuators A: Physical*, Vol. 165, No. 2, 2011, pp. 351-366.
- [50] L. Oren, and E. Gutmark, "Flow Characteristics of Non Circular Synthetic Jets," *47th AIAA Aerospace Sciences Meeting*, 5-8 January 2009, Orlando, Florida.
- [51] R. Q. Shan, J. J. Wang, "Experimental Studies of the Influence of Parameters on Axisymmetric Synthetic Jets," *Sensors and Actuators*, Vol. 157, 2010, pp. 107-112.
- [52] Q. Gallas, R. Holman, T. Nishida, B. Carroll, M. Sheplak and L. Cattafesta, "Lumped Element Modeling of Piezoelectric-driven Synthetic Jet Actuators," *AIAA Journal*, Vol. 41, 2003, No. 2, pp. 240-247
- [53] S. O. Jun, Y. H. Jeon, J. H. Rho and D. H. Lee, "Application of Collaborative Optimization Using Genetic Algorithm and Response Surface Method to an Aircraft Wing Design," *Journal of Mechanical Science and Technology*, Vol. 20, 2006, No. 1, pp. 133-146.
- [54] S. O. Kang, S. O. Jun, K. H. Park, Y. H. Jeon and D. H. Lee, "Study of Neural Network Training Algorithm Comparison and Prediction of

- Unsteady Aerodynamic Forces of 2D Airfoil,” *Journal of the Korean Society for Aeronautical and Space Science (KSAS)*, Vol. 27, 2009, No. 5, pp. 425-432.
- [55] J. A. Freeman and D. M. Skapura, “Neural Networks Algorithm, Applications, and Programming Techniques,” Addison-Wesley Publishing Company, 1992.
- [56] G. N. Vanderplaats and S. R. Hansen, “DOT User Manual,” VMA Engineering, Goleta, CA, 1989.
- [57] J.-F. Beaudoin and J.-L. Aider, “Drag and Lift Reduction of a 3D Bluff Body using Flaps,” *Experiments in Fluids*, Vol. 44, 2008, pp. 491-501.
- [58] Y. H. Kim and K. P. Garry, “Optimization of a Rectangular Orifice Synthetic Jet Generator,” *3rd AIAA Flow Control Conference*, 5-8 June 2006, San Francisco, California
- [59] H. I. Park, Y. B. Lee, S. O. Kang, J. W. Lee, K. H. Kim, and D. H. Lee, “Shape Optimization of Piezo-actuated Synthetic Jet for Active Flow Control,” *6th National Congress on Fluid Engineering*, 18-20 August 2010, Busan, Korea.
- [60] K. R. Cooper, Bluff-Body Aerodynamics as Applied to Vehicles, *J. Wind Engineering and Industrial Aerodynamics*, 49 (1993) 1-22
- [61] F.-R. Grosche, and G.E.A. Meier, “Research at DLR Gottingen on Bluff Body Aerodynamics, Drag Reduction by Wake Ventilation and Active Flow Control,” *Journal of Wind Engineering and Industrial Aerodynamics*, Vol. 89, 2001, 1201-1218.

초 록

본 연구에서는 최근 후류 능동제어 기술로 각광받고 있는 합성제트(Synthetic jet)에 대한 실험적 연구를 수행하였다. 먼저, 합성제트 구동기(Synthetic jet actuator)의 형상과 구동조건에 따른 매개변수 연구와 최적설계를 수행하였다. 그리고 단순화 된 자동차 형상의 대표적인 기준형상인 Ahmed 차체모델에 합성제트를 적용하여 공기저항 저감을 위한 후류 능동제어 실험을 하였다.

합성제트 구동기의 성능은 발생 제트의 유속 크기로 나타낼 수 있고, 이는 합성제트 구동기의 형상과 구동신호의 영향을 받는다. 본 연구에서는 각각 5, 10, 15 mm 의 합성제트 구동기 분출구 길이와 공동 깊이에 따라 총 9가지의 합성제트 구동기를 설계/제작 하였으며, 구동 주파수에 따라 유속측정 실험을 수행하였다. 그 결과, 큰 유속이 발생하는 두 주파수 영역이 발견되었으며, 이는 공동의 공진과 진동판의 공진에 기인한다. 진동판의 공진 주파수에서 진동판을 구동시키는 것은 파손을 야기할 수 있기 때문에, 합성제트의 속도를 최대화 시키기 위해서는 공동 공진 현상을 적절히 이용할 필요가 있다. 분출구 길이와 공동 깊이에 따른 유속측정 실험 결과, 대부분 형상에서 공동 공진 주파수라 여겨지는 한 주파수에서 최대속도가 발생하였고, 이 주파수는 형상에 따라 다르게 나타났다. 한편, 5 mm 로 공동의 깊이가 작은 경우 공동 공진 주파수 이후에도 유속이 작아지지 않고 오히려 유속이 약간 증가하는 현상이 발견되었다. 일반적으로 분출구의

길이와 공동의 깊이가 작을수록 해당 형상에서 최대유속이 커지는 것으로 나타났으나, 최적화 수행 결과 분출구의 길이에 대하여는 최적의 길이가 존재하였다.

또한, 합성제트를 Ahmed 차체모델에 적용하여 합성제트의 여러 조건에 따른 풍동 실험을 수행하였다. 배열형태로 12개의 합성제트를 발생시켰으며, 이를 25도와 35도 후면 경사각을 갖는 두 Ahmed 차체모델에 적용하였다. 합성제트는 천장의 뒤쪽 끝 부분이나 경사면의 양쪽 옆면에서 분출되었고, 합성제트의 방향, 세기, 구동 주파수, 배열 내에서 합성제트 구동기 분포에 따라 공기저항을 측정하여 그 경향성을 파악하였다. 또한, 후면 압력 측정과 유동가시화 실험을 통해 합성제트 분출에 따른 후류의 변화를 관찰하고자 하였다. 결과로부터, Ahmed 차체모델의 공기저항은 모델의 경사각과 합성제트의 발생 위치에 따라 감소하거나 증가하였다. 25도 경사각 모델의 천장 끝에서 합성제트가 분출된 경우 공기저항이 감소하였고 (최대 5.2%), 경사면의 양쪽 옆면에서 분출된 합성제트는 공기저항과 후류에 영향을 미치지 않았다. 한편, 35도의 경사각 모델의 경우 합성제트의 분출에 의해 공기저항이 오히려 증가하였으며, 특히 천장 끝에서 합성제트가 분출된 경우 강한 말굽꼴 와류가 유도되면서 공기저항이 크게 증가하였다 (20% 이상). 공기저항이 줄어든 경우 (25도 경사각 모델 천장 끝에서 합성제트가 작동했을 때), 합성제트의 강도가 세거나 제트의 방향이 자유류에 가까울수록 공기저항이 많이 줄어들었고, 구동 주파수는 공기저항 저감에 큰 영향을 미치지 않았다. 또한 적은 개수의 합성제트 구동기가 작동할 경우 전체 공기저항 감소량은 줄어들었으나, 천장 끝의 중앙에서

작동한 경우 단위 개수당 공기저항 감소량이 증가하여 효율적으로 공기저항이 저감되었다. 본 연구로부터 합성제트를 이용하여 자동차의 후류를 제어하여 공기저항을 저감시킬 수 있음을 확인하였고, 공기저항을 저감시킬 수 있는 합성제트의 설치, 구동 조건에 대하여 알 수 있었다. 또한, 적절하지 않은 합성제트 적용은 공기저항을 크게 증가시킬 수 있다는 것을 알 수 있었다.

주요어: 능동 유동 제어, 합성제트, 아메드 차체형상, 공기저항 저감, 풍동 실험

학 번 : 2008-20747

성 명 : 박 훈 일